Hierarchy of coherent vortices in developed turbulence

Susumu Goto and Yutaro Motoori

Graduate School of Engineering Science, Osaka University, 1-3, Machikaneyama, Toyonaka, 560-8531, Osaka, Japan.

*Corresponding author(s). E-mail(s): s.goto.es@osaka-u.ac.jp; y.motoori.es@osaka-u.ac.jp;

Abstract

We review our recent studies on the hierarchy of coherent vortices in high-Reynolds-number turbulence of an incompressible neutral fluid, which were conducted through analyses of data obtained by direct numerical simulations of the Navier–Stokes equation. We show results on turbulence under four different boundary conditions: namely, turbulence in a periodic cube, turbulent wake behind a circular cylinder, turbulence between a pair of parallel planes (i.e. turbulent plane Poiseuille flow), and a zero-pressure gradient turbulent boundary layer. By decomposing each of these turbulent fields into different length scales, we show that turbulence is composed of the hierarchy of coherent vortices with different sizes. More concretely, in a region apart from solid walls, each level of the hierarchy consists of tubular vortices and they tend to form counter-rotating pairs. It is a strain-rate field around them that stretches and amplifies smaller vortices. In other words, the energy cascade in turbulence away from walls is not caused by breakups of larger eddies, but vortex stretching of smaller eddies in larger-scale strain-rate fields. In near-wall regions, the sustaining mechanism of vortices depends on their scale, which we need to consider depending on the distance from a wall. Large vortices (i.e. wall-attached eddies), whose diameter is as large as the distance from a wall, are sustained by the mean-flow stretching, whereas smaller vortices (i.e. wall-detached eddies), whose diameter is smaller than the distance, are created by being stretched by larger vortices. The latter mechanism corresponds to the energy cascade similarly observed in wall-free turbulence. Scale decomposition can also reveal the largest vortices in each turbulence, which depends on the boundary condition. It is particularly important that the largest wall-attached eddies in the turbulent boundary layer are hairpin vortices even in downstream regions.

1 Introduction

1.1 Kolmogorov similarity and energy cascade

The Reynolds number defined as

$$Re = U_0 L_0 / \nu \tag{1}$$

determines flow state under a fixed flow condition. Here, ν, U_0, and L_0 denote the kinematic viscosity of the fluid, the representative velocity and length of the boundary condition or the external forcing. In general, when Re is larger than a few thousands, flow becomes turbulent; and for larger Re, turbulence becomes fully developed. The energy spectrum $E(k)$ of developed turbulence is broad over a range of wavenumber k. More precisely, according to Kolmogorov (1941)'s similarity hypothesis (Frisch, 1995, § 6), the energy spectrum obeys a power-law,

$$E(k) = C\, \bar{\epsilon}^{\frac{2}{3}}\, k^{-\frac{5}{3}}\,, \tag{2}$$

in the wavenumber range

$$2\pi/L \ll k \ll 2\pi/\eta \qquad \text{(inertial range)} \tag{3}$$

corresponding to the length-scale range between the viscous scale (i.e. the Kolmogorov length),

$$\eta = \bar{\epsilon}^{-\frac{1}{4}}\, \nu^{\frac{3}{4}}\,, \tag{4}$$

where $\bar{\epsilon}$ denotes the average dissipation rate of the turbulent kinetic energy per unit mass, and the velocity correlation length (i.e. the integral length), L. The constant C in (2) is called the Kolmogorov constant, which is universal irrespective of the kinds of turbulence (Sreenivasan, 1995).

The power law (2) of the energy spectrum implies that developed turbulence is statistically self-similar in scales between η and L, and it is composed of vortices with various sizes. By substituting Taylor (1935)'s dissipation law (Tennekes and Lumley, 1972, § 1.5),

$$\bar{\epsilon} \sim u'^3 / L\,, \tag{5}$$

where u' is the standard deviation of a component of turbulent velocity, into (4), we express the scale ratio between the largest and smallest scales as

$$L/\eta \sim Re^{\frac{3}{4}} \tag{6}$$

in terms of the Reynolds number Re. Here, we define Re, (1), by using u' and L for U_0 and L_0, respectively. The relation (6) means that the number of levels in the hierarchy of vortices increases with Re.

We usually understand that the origin of Kolmogorov (1941)'s similarity is in the so-called energy cascade. Richardson (1922, p. 66)'s famous verse,

> *big whirls have little whirls that feed on their velocity, and little whirls have lesser whirls and so on to viscosity,*

adequately describes the cascade (i.e. inter-scale transfer) of energy in turbulence: that is, energy injected by external force or mean flow to largest scales (i.e. the integral length L) transfers to smaller scales in a scale-by-scale manner, and the energy reached at the smallest scale (i.e. the Kolmogorov length η) is dissipated due to the viscosity. Since Richardson (1922)'s verse gives only qualitative description of the energy cascade, there were numerous studies on the process. For example, it was numerically shown that the energy transfers from low-wavenumber Fourier modes to higher-wavenumber modes in turbulence in a periodic cube (Domaradzki and Rogallo, 1990; Ohkitani and Kida, 1992). It is also well-known that the cascade models such as shell models (Yamada and Ohkitani, 1987; Biferale, 2003), which were developed to mimic the energy transfer in the wavenumber space, successfully describe important statistics of turbulence such as Kolmogorov's similarity and its corrections due to intermittency (Frisch, 1995, Chap. 8).

1.2 Mechanisms of energy cascade in real space

As mentioned above, Kolmogorov (1941)'s similarity is explained by the concept of energy cascade, i.e. the scale-by-scale energy transfer from larger to smaller scales in turbulence. Although many researchers tried to reveal a concrete image of the hierarchy of vortices of various sizes, which is described by Richardson (1922)'s verse and depicted by the frequently used schematic (Frisch, 1995, Fig. 7.2), and to explain the physical mechanism of energy cascade, there is still a large room to conclude its elementary mechanism in real space (Sagaut and Cambon, 2018, § 4.11.2). In fact, several mechanisms describing energy cascade have been proposed, and here we summarize them.

First, we introduce the mechanism in terms of vortex stretching. Since Taylor (1938) pointed out the importance of vortex stretching in turbulence generation, the picture of energy cascade by vortex stretching has been a classical view. For example, the textbook by Tennekes and Lumley (1972, § 8.2) describes energy cascade in terms of this mechanism. Furthermore, recent direct numerical simulations (DNS), in which the equation of motion for fluid is numerically integrated without modeling, helped us to demonstrate the evidence that vortex stretching contributes to the cascade (Davidson et al, 2008; Leung et al, 2012; Lozano-Durán et al, 2016; Doan et al, 2018). We also conducted a series of studies (Goto, 2008, 2012; Goto et al, 2017) from this viewpoint. Although this mechanism seems reasonable as described in the rest of the present article, there is no consensus that this is the only mechanism describing the cascade (Davidson, 2004, § 5.1.2).

Another important picture of the energy cascade is due to vortex reconnections. Since smaller vortices can be created during the reconnection of a counter-rotating pair of vortex tubes, this may be a primary mechanism of the cascade. Hussain and his coworkers have developed this picture since the last century (Melander and Hussain, 1988; Hussain and Duraisamy, 2011; Yao and Hussain, 2020), and, in particular, Yao and Hussain (2020) recently showed by DNS that successive reconnections can lead to the energy cascade. Brenner et al (2016) also referred to this mechanism in the study on the singularity formation in an inviscid fluid. In laboratory experiments on the collision of two vortex rings (McKeown et al, 2018, 2020) and the related study

(McKeown et al, 2023), concrete processes of vortex reconnections on different scales were captured. Furthermore, Kerr (2013) also suggested another mechanism of the cascade in terms of vortex reconnections.

Here, it is important to note that the strain rate, rather than the vorticity, is responsible for the energy flux and dissipation. In fact, Tsinober (2001, Chap. 6) pointed out the importance of amplification of not only the vorticity but also the strain rate, and several recent studies (Paul et al, 2017; Carbone and Bragg, 2020; Johnson, 2020; Vela-Martín and Jiménez, 2021) claimed the importance of the strain-rate self-amplification. However, this is also under debate as Johnson (2021) concluded that the strain-rate amplification and the vortex stretching are equally important for inter-scale energy transfer.

1.3 Current status of DNS of turbulence

The preceding subsection describes that there is no consensus on the physical mechanism of energy cascade in real space. However, this situation is changing in recent years as DNS studies of turbulence have led to more detailed data analysis [see Yao et al (2024) for a recent example]. Since, in principle, DNS can provide time-series of three-dimensional structures and detailed information on interactions between scales, we expect that the actual hierarchy of vortices and the physical mechanism of energy cascade will be understood in the near future.

We have emphasized at the beginning of this article that the Reynolds number characterizes flow. Therefore, the current status of DNS study of turbulence is also quantified by the Reynolds number. However, Re in (1) is defined in terms of the velocity and length scale characterizing boundary conditions or external force. It is therefore more appropriate that we use another Reynolds number characterizing the state of turbulence to quantify its degree of development. In this subsection, we introduce the appropriate definition of Reynolds number for each of four kinds of turbulent flows treated in the present article, and show the achievement of the state-of-the-art DNS of turbulence. In addition to this, basic concept of turbulence is also summarized so that even non-experts can understand discussion in the following.

1.3.1 Turbulence in a periodic cube

First, we describe DNS of turbulence in the simplest case: namely, statistically homogeneous isotropic turbulence under periodic boundary conditions in three orthogonal directions. The first DNS of this kind of turbulence was conducted by Orszag and Patterson (1972). For a half century since then, many DNS of the turbulence at higher and higher Re were conducted thanks to the continuous development of supercomputers. In particular, at the beginning of the present century, Kaneda et al (2003) conducted the DNS of the turbulence by the spectral method (see § 2.1) using a large number 4093^3 of Fourier modes. Then, they numerically realized turbulence at the Taylor-length Reynolds number, which is defined as

$$Re_\lambda = u'\lambda/\nu \tag{7}$$

with the Taylor length

$$\lambda = \sqrt{15\nu u'^2/\overline{\epsilon}}\,, \tag{8}$$

to be $Re_\lambda \approx 1000$. Recently, Ishihara et al (2020) conducted further larger DNS with 12288^3 Fourier modes to simulate turbulence at $Re_\lambda = 2250$.

Substituting Taylor (1935)'s dissipation law (5) into (8), we obtain $\lambda \sim \sqrt{L\nu/u'}$. Then, substituting this into (7), we can see that Re and Re_λ are related by

$$Re \sim {Re_\lambda}^2\,. \tag{9}$$

Since the scale separation L/η in the inertial range gets larger as Re increases [see (6)], Re_λ also indicates the width of the inertial range (3). Though the definition of Re depends on boundary conditions, the Taylor length λ, and therefore Re_λ, can be estimated according to flow state. Hence, Re_λ appropriately indicates the development of turbulence. In fact, according to Dimotakis (2000), turbulence is accompanied with a sufficient scale separation when

$$Re_\lambda \gtrsim 100\text{–}140\,. \tag{10}$$

Therefore, we call the flow satisfying (10) developed turbulence. In this review, we show results of the analysis of turbulence which satisfies (10).

1.3.2 Free shear flow turbulence

Turbulence in a periodic box is artificial flow which is a model of flow away from solid walls. Numerous DNS of more realistic turbulence were also conducted. Turbulent wake, which is sustained behind an obstacle immersed in uniform flow, is an extensively studied example of free shear flows. In fact, DNS and large-eddy simulations (LES) (Tomboulides et al, 1993) of turbulent wake behind a circular cylinder were already conducted in 1990's. At the beginning of the present century, Ma et al (2000) conducted the DNS of developed turbulence in the wake behind a cylinder at the Reynolds number

$$Re_D = U_\infty D/\nu \tag{11}$$

defined by the uniform upstream velocity U_∞ and cylinder diameter D to be $Re_D = 3900$. Since then, many DNS were conducted and we also conducted DNS of turbulence at $Re_D = 5000$ (Fujino et al, 2023). In this article, we review results of this DNS. As will be shown in § 2.2 (see Fig. 3), the Taylor-length Reynolds number (7) in this turbulence exceeds 100 within the distance $10D$ behind the cylinder. Thus, it satisfies the criterion (10), which is discussed in the previous subsection, of developed turbulence, and we expect that there is a hierarchy of vortices in the simulated turbulence.

1.3.3 Wall turbulence

Numerous DNS of turbulence near a solid wall were conducted. In particular, turbulence between a pair of parallel planes (i.e. turbulent plane Poiseuille flow), which we call the turbulent channel flow in the following, has been intensively studied as one of

the canonical wall-bounded turbulence. For channel flow, the Reynolds number (1) is defined by using the central velocity U_c and the channel half width h in the places of U_0 and L_0 as

$$Re_h = U_c h/\nu\,. \tag{12}$$

Though the critical Reynolds number for the linear instability of the laminar flow is $Re_h = 5772$ (Orszag, 1971), it is known that turbulence is sustained at even lower Re_h. The DNS of turbulent channel flow was first conduced by Kim et al (1987) at $Re_h = 3300$. Since then, many authors conducted DNS. In this century, DNS of turbulent channel flow at high Reynolds numbers became possible (Abe et al, 2001; del Álamo and Jiménez, 2003; Tanahashi et al, 2004), Jiménez and his coworkers have been extensively conducting large-scale DNS (del Álamo and Jiménez, 2003; del Álamo et al, 2004; Hoyas and Jiménez, 2006; Lozano-Durán and Jiménez, 2014; Hoyas et al, 2022).

We define x and y axes in the streamwise and wall-normal directions, respectively [Fig. 2(b)] to introduce the friction velocity as

$$u_\tau = \sqrt{\nu \left.\frac{\partial \overline{u}_x}{\partial y}\right|_{\text{wall}}}\,. \tag{13}$$

Here, $\overline{\boldsymbol{u}}$ denotes the mean velocity, and in the following we denote the fluctuation velocity by $\widetilde{\boldsymbol{u}}$ $(= \boldsymbol{u} - \overline{\boldsymbol{u}})$. Then, the friction Reynolds number defined as

$$Re_\tau = u_\tau h/\nu \tag{14}$$

is an indicator of the hierarchy of vortices in wall turbulence. This is because Re_τ is the scale ratio between the smallest length in the vicinity of solid walls (i.e. the friction length $\ell_\tau = \nu/u_\tau$) and the size of the largest structure in the flow (i.e. the channel half width h); namely, $Re_\tau = h/\ell_\tau = h^+$. Hereafter, superscript $^+$ denotes the length normalized by ℓ_τ.

It is known (Tennekes and Lumley, 1972, § 5.2) that in wall turbulence at sufficiently high Re_τ, the mean streamwise velocity $\overline{u}_x$ normalized by the friction velocity is a linear function of $\log y^+$ as

$$\overline{u}_x/u_\tau = B + \kappa^{-1}\,\log y^+ \tag{15}$$

in the layer

$$30\text{–}100 \lesssim y^+ \lesssim 0.2h^+ = 0.2Re_\tau \qquad \text{(logarithmic layer)}\,. \tag{16}$$

In (15), B and $\kappa(\approx 0.4)$ are constants and the latter is called the Kármán constant. In the near-wall region (i.e. $5 \lesssim y^+ \lesssim 30$–$100$, which is called the buffer layer), there is only single-scale structures, whereas there exists multiple scales in the logarithmic layer, in particular, for large y^+. This can be understood, if we recall that the largest eddies at the distance y from the wall are as large as y, and that the smallest eddies are as small as the Kolmogorov length η, (4). Note that we may estimate η as a function

of y as follows. To this, we estimate the mean energy dissipation rate $\overline{\epsilon}$ at the distance y from the wall, under the assumption that it is balanced with the energy input rate. Then, in the logarithmic layer (16),

$$\overline{\epsilon} \approx -\overline{\widetilde{u}_x \widetilde{u}_y} \frac{\partial \overline{u}_x}{\partial y} \approx -\frac{u_\tau^3}{\kappa y} \,. \tag{17}$$

Therefore, we may estimate the Kolmogorov length (4) normalized by the friction length ℓ_τ as

$$\eta^+ \approx (\kappa y^+)^{\frac{1}{4}} \,. \tag{18}$$

See Fig. 4 in § 2.3 for numerical evidence of the estimation (18). Hence, the scale ratio between the largest ($L \approx y$) and smallest (η) eddies at the distance y from the wall is estimated as $L/\eta \approx \kappa^{-\frac{1}{4}} (y^+)^{\frac{3}{4}}$. Since $\kappa^{-\frac{1}{4}} \approx 1.3$, $L/\eta = 16$–40 at the bottom $y^+ = 30$–100 of the logarithmic layer. Recalling that the diameter of the smallest eddies is about 10η, we may see that there exists a hierarchy of vortices in the logarithmic layer (16). Since the layer enlarges, in wall unit, with Re_τ, we expect clearer hierarchical structures at higher Reynolds numbers.

The Reynolds number of turbulent channel flow achieved by DNS was $Re_\tau = 550$ (del Álamo and Jiménez, 2003) about 20 years ago, $Re_\tau = 2003$ (Hoyas and Jiménez, 2006) about 15 years ago, $Re_\tau = 4200$ (Lozano-Durán and Jiménez, 2014) about 10 years ago. Recently, it further increases, and Yamamoto and Tsuji (2018) conducted DNS at $Re_\tau = 8000$ and Hoyas et al (2022) at $Re_\tau = 10000$. Through these large DNS, the scale separation in the turbulence gets much clearer, and coexistence of large flow structures experimentally known as the (very) large scale motion (Kim and Adrian, 1999) and fine-scale structures are also captured by DNS. In other words, data for the investigation of the hierarchy of vortices are available. In this article, we review our analysis (Motoori and Goto, 2021) of the data at $Re_\tau = 4200$ obtained by Lozano-Durán and Jiménez (2014).

Another intensively investigated wall turbulence is the boundary layer on a flat plane. In this article, we investigate a turbulent boundary layer developing on a plane when uniform flow at the velocity U_∞ exists in the direction parallel to the plane. Since the seminal DNS by Spalart (1988) in the last century, many researchers conducted DNS of this canonical flow. Since the boundary layer thickness, which is often defined by the momentum thickness θ, develops in downstream, the Reynolds number (1) defined by θ,

$$Re_\theta = U_\infty \theta / \nu \,, \tag{19}$$

also increases in downstream. It is numerically shown by Schlatter and Örlü (2010) that Re_θ and Re_τ are related as $Re_\tau = 1.13 \times Re_\theta^{0.843}$. At the beginning of this century, large DNS were conducted by Komminaho and Skote (2002) ($Re_\theta \lesssim 750$) and Khujadze and Oberlack (2004) ($Re_\theta \lesssim 2800$). Since then, the Reynolds number of turbulent boundary layer achieved by DNS is increasing, and the recent DNS are $Re_\theta \lesssim 6680$ (Sillero et al, 2013) and $Re_\theta \lesssim 8300$ (Eitel-Amor et al, 2014), which correspond to $Re_\tau \lesssim 2000$ and $Re_\tau \lesssim 2300$, respectively. Thus, we can obtain DNS data of developed turbulent boundary layers in which, similarly to the turbulent channel flow, we may expect hierarchical structures of vortices with different sizes in the logarithmic layer.

We also conducted DNS of turbulent boundary layer at $Re_\theta \lesssim 4600$, which correspond to $Re_\tau \lesssim 1380$ and $Re_\lambda \lesssim 75$ (Motoori and Goto, 2020). In the following sections, we show results of the analysis of this DNS data. There is also a dispute, which is related to the hierarchy of vortices, on the largest-scale vortices in turbulent boundary layer. It was experimentally shown by many authors (Head and Bandyopadhyay, 1981; Adrian et al, 2000) that largest-scale eddies in the developed turbulent boundary layer are hairpin-shaped. However, in DNS, the existence of large-scale hairpin-like structures ware not emphasized. On the contrary, there were studies (Schlatter et al, 2014, e.g.) to conclude that hairpin vortices disappear in downstream region of high-Reynolds-number turbulence. Hence, there is a room for better understanding the hierarchy of vortices in turbulent boundary layers.

1.4 Aim of this article

As described in § 1.3, many DNS of developed turbulence at sufficiently high Reynolds numbers in canonical flow geometries have been already conducted. Nevertheless, as mentioned in § 1.2, there is no consensus on the concrete image and sustaining mechanism of the hierarchy of vortices in developed turbulence. This situation is partly caused by the fact that we cannot capture the hierarchy of vortices by simply using the vorticity, the squared vorticity (i.e. enstrophy), or the second invariant of the velocity gradient tensor, for example. We explain in detail this point in § 3. To overcome this situation, we have been developing simple methods to identify the hierarchy of vortices and to investigate its sustaining mechanism (i.e. energy cascade) in the series of our studies (Goto, 2008, 2012; Goto et al, 2017; Motoori and Goto, 2019, 2020, 2021; Fujino et al, 2023). Therefore, the aim of this article is to review our studies in a unified manner. To this end, in the following, we review our knowledge, which was obtained through the data analysis of DNS, on the concrete pictures and the sustaining mechanism of the hierarchy of coherent vortices in four different kinds of turbulence: namely, turbulence in a periodic cube (Goto, 2008, 2012; Goto et al, 2017), turbulent wake behind a circular cylinder (Fujino et al, 2023), turbulence between a pair of parallel plates Motoori and Goto (2021), and zero-pressure gradient turbulent boundary layer on a flat plate (Motoori and Goto, 2019, 2020).

2 Direct numerical simulations

In this section, we summarize the numerical methods and parameters of DNS and basic statistics of simulated turbulence in the four different geometries.

2.1 Turbulence in a periodic cube

For turbulence in a periodic cube, we numerically integrate the Navier–Stokes equation,

$$\frac{\partial \boldsymbol{u}}{\partial t} + \boldsymbol{u}\cdot\boldsymbol{\nabla}\boldsymbol{u} = -\frac{1}{\rho_f}\,\boldsymbol{\nabla} p + \nu\nabla^2\boldsymbol{u} + \boldsymbol{f}\,, \tag{20}$$

and the continuity equation,

$$\boldsymbol{\nabla}\cdot\boldsymbol{u} = 0 \tag{21}$$

under periodic boundary conditions in all the three orthogonal directions. We use the Fourier spectral method (Canuto et al, 2006, § 3.3). The advantage of the spectral method is that we can precisely estimate spatial derivatives and integrate (20) with the solenoidal condition (21) being accurately satisfied.

The concrete numerical procedure is as follows. We numerically solve the vorticity equation,

$$\frac{\partial \boldsymbol{\omega}}{\partial t} + \boldsymbol{u} \cdot \boldsymbol{\nabla} \boldsymbol{\omega} = \boldsymbol{\omega} \cdot \boldsymbol{\nabla} \boldsymbol{u} + \nu \, \nabla^2 \boldsymbol{\omega} + \boldsymbol{\nabla} \times \boldsymbol{f} \, , \tag{22}$$

which is the rotation of the Navier–Stokes equation (20). Here,

$$\boldsymbol{\omega} = \boldsymbol{\nabla} \times \boldsymbol{u} \tag{23}$$

is the vorticity field. By using (21), we rewrite the nonlinear terms in (22) as

$$\frac{\partial \omega_i}{\partial t} = -\epsilon_{ijm} \frac{\partial^2 u_m u_\ell}{\partial x_j \partial x_\ell} + \nu \, \nabla^2 \omega_i + \epsilon_{ijm} \frac{\partial f_m}{\partial x_j} \, . \tag{24}$$

Here, we denote the Fourier transforms of the velocity and vorticity fields as $\widehat{\boldsymbol{u}}(\boldsymbol{k}, t)$ and $\widehat{\boldsymbol{\omega}}(\boldsymbol{k}, t)$, respectively. Then, since the former can be expressed by the latter as

$$\widehat{\boldsymbol{u}} = \mathrm{i} \, \boldsymbol{k} \times \widehat{\boldsymbol{\omega}} / k^2 \, , \tag{25}$$

the Fourier transform of the vorticity equation (24) is closed only by $\widehat{\boldsymbol{\omega}}$. Thus, we numerically integrate it by the fourth-order Runge–Kutta–Gill method. In the Fourier spectral method, we compute the nonlinear terms in (24) in real space, by using the fast Fourier transform (FFT), instead of computing it through the estimation of the convolution in wavenumber space. In this procedure, we remove the aliasing errors by the combination of the phase shift and spherical truncation (Canuto et al, 2006, § 3.3.2).

In this article, we show results of DNS of turbulence driven by two different kinds of external forces. The first one (Goto et al, 2017) is steady force expressed as

$$\boldsymbol{f}^{(v)} = \begin{pmatrix} -\sin x \cos y \\ +\cos x \sin y \\ 0 \end{pmatrix} \, . \tag{26}$$

This force drives a four parallel vortex tubes, whose axis is parallel to z direction, in a periodic cube. In fact, when the Reynolds number is low, the flow becomes steady flow with these vortex columns, which we call the Taylor–Green vortices in this article. As will be seen in § 4.1, even in turbulence at higher Reynolds numbers, these Taylor–Green vortices exist at fixed positions. Although this is advantageous to investigate the hierarchy of coherent vortices, it is difficult to examine its universality only with this specific forcing. Thus, we also examine another case of turbulence in a periodic cube

with another force (Lamorgese et al, 2005), whose Fourier transform is expressed as

$$\widehat{\boldsymbol{f}^{(i)}}(\boldsymbol{k},t) = \begin{cases} \dfrac{P}{2E_f(t)}\,\widehat{\boldsymbol{u}}(\boldsymbol{k},t) & \text{if } \ 0<|\boldsymbol{k}|\le k_f, \\ 0 & \text{otherwise.} \end{cases} . \tag{27}$$

Here,

$$E_f = \sum_{0<|\boldsymbol{k}|\le k_f} \frac{1}{2}\,|\widehat{\boldsymbol{u}}|^2 \tag{28}$$

is the energy contained in the forcing wavenumber range ($0 < |\boldsymbol{k}| \le k_f = 2.5$). By construction, the energy input rate P due to this force is constant in time; we set $P = 0.1$ in our DNS. It is important that the forcing is statistically homogeneous and isotropic and therefore it induces no specific coherent structures at the forcing scale. In other words, coherent structures observed in turbulence driven by (27) are all self-organized.

Since the aim of DNS is to show the hierarchy of vortices in turbulence, it is important to resolve the smallest scale eddies. When we use N Fourier mode in each direction, the maximum wavenumber $k_{\max}$ is $\sqrt{2}N/3$ because of the de-aliasing method (Canuto et al, 2006, § 3.3.2). The resolution of the Fourier spectral method is often evaluated by the product of $k_{\max}$ and the Kolmogorov length η. Since the diameter of the smallest eddies is known to be about 10η (see Fig. 5 in § 3), and since the numerical resolution is $2\pi/k_{\max}$, $k_{\max}\eta$ must be larger than 1 so that such small eddies are well resolved. Therefore, we appropriately choose the kinematic viscosity ν so that this condition is satisfied for the given number N^3 of Fourier modes. In the following, we show the DNS results with $N^3 = 1024^3$ and $k_{\max}\eta = 1.4$ for forcing (26) and $k_{\max}\eta = 1.5$ for forcing (27). Accordingly, the Taylor-length Reynolds number (7) is 250 and 330 for each forcing scheme. These values sufficiently satisfy the criterion (10) of the developed turbulence.

To further verify the development of the simulated turbulence, we plot the energy spectrum in Fig. 1 with solid curves; thin and thick lines correspond to the cases with forcing (26) and forcing (27), respectively. In this figure, we show the one-dimensional longitudinal spectrum $E_\parallel$ [1]. Since $E_\parallel$ is expressed as

$$E_\parallel(k_1) = \frac{1}{2}\int_{k_1}^{\infty} \frac{E(k)}{k}\left(1-\frac{k_1^2}{k^2}\right) dk \tag{30}$$

in terms of the (three-demoniacal) spectrum E (Batchelor, 1953, p 50), we evaluate $E_\parallel$ through (30). Since the derivative of (30) leads to $E(k) = k^3 d(k^{-1}dE_\parallel/dk)/dk)$,

[1] We use the definition of $E_\parallel$ as

$$\frac{1}{2}u'^2 = \int_0^\infty E_\parallel(k)dk\,, \tag{29}$$

which is different from ϕ_1 adopted by Sreenivasan (1995) with a factor 2; $\phi_1 = 2E_\parallel$.

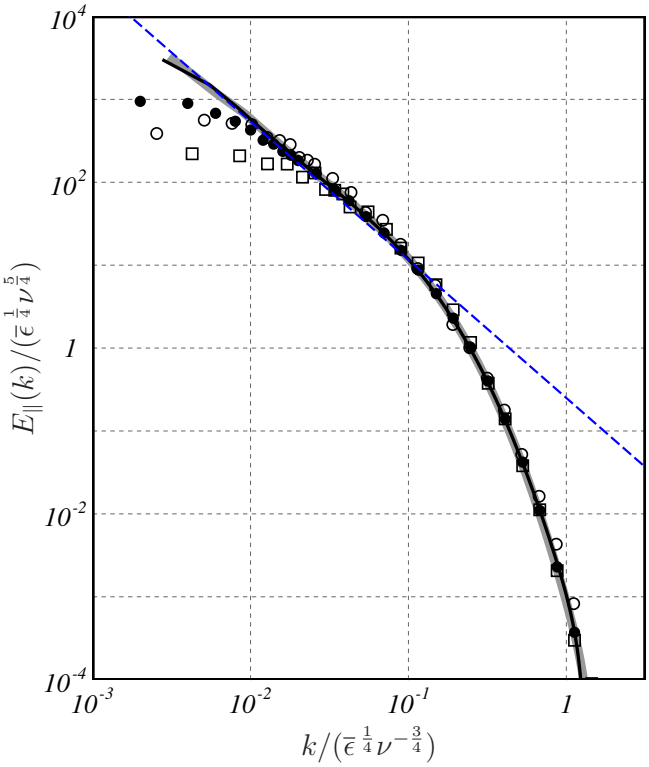

Fig. 1 One-dimensional longitudinal energy spectrum $E_{\parallel}$, (29), of four different kinds of turbulence: thin and thick lines, turbulence in periodic cube driven by (26) and (27), respectively; ●, turbulent channel flow at the wall-normal location $y^+ = 630 \approx 0.15h^+$; ◯, turbulent wake behind a cylinder at the streamwise location $(x/D = 1)$; □, turbulent boundary layer at the streamwise location corresponding to Re_θ =3600 and the wall-normal location $y^+ = 165 \approx 1.2\theta^+$. For turbulence in a periodic cube, we use (30) to estimate $E_{\parallel}$ from E, while for the other kinds of turbulence, we estimate $E_{\parallel}$ by the Fourier transform in z direction of z component $\widetilde{u}_z$ of the fluctuating velocity; see Fig. 2 for the definition of the coordinate. Blue dashed line indicates power-law spectrum, $E_{\parallel}(k) = 0.25\bar{\epsilon}^{\frac{2}{3}}k^{-\frac{5}{3}}$.

$E_{\parallel}$ is expressed as

$$E_{\parallel}(k) = \frac{9C}{55}\,\bar{\epsilon}^{-\frac{2}{3}}k^{-\frac{5}{3}} \qquad \left(\Leftrightarrow \quad \frac{E_{\parallel}}{\bar{\epsilon}^{\frac{1}{4}}\nu^{\frac{5}{4}}} = \frac{9C}{55}\,\frac{k}{\bar{\epsilon}^{\frac{1}{4}}\nu^{-\frac{3}{4}}} \right) \tag{31}$$

in the inertial range (3). The dotted blue line in Fig. 1 denotes this power law with the coefficient $\frac{9C}{55} = 0.25$. We have chosen this value according to the experimental value Sreenivasan (1995) of the Kolmogorov constant. The Reynolds number Re_λ is large enough for the spectrum to obey a power law which is consistent with the Kolmogorov spectrum (31) for $k \lesssim 0.1\eta^{-1}$. Therefore, we expect a self-similar hierarchy of vortices in the corresponding length scales.

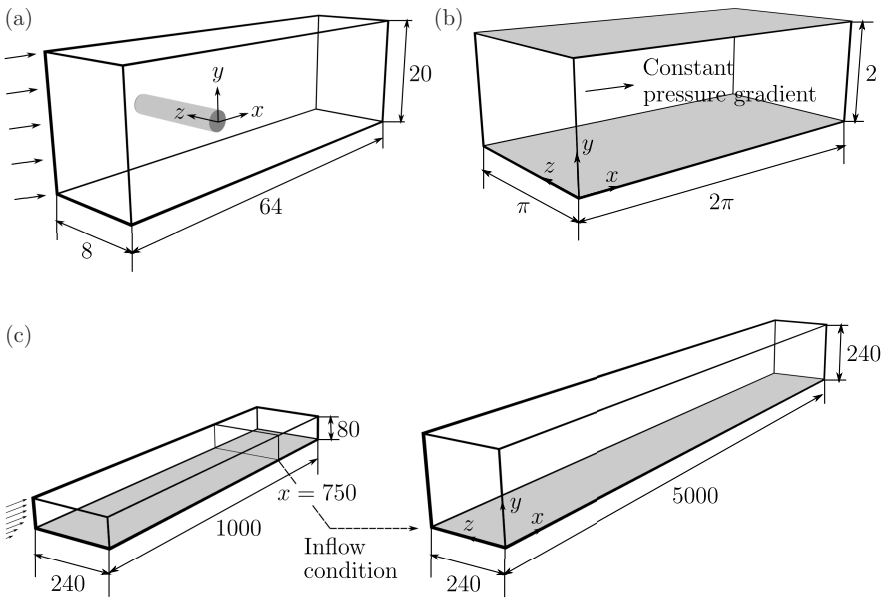

Fig. 2 Configuration of DNS of (a) turbulent wake behind cylinder, where the length is normalized by cylinder diameter D, (b) turbulent channel flow, and (c) turbulent boundary layer, where the length is normalized by the displacement thickness at the inlet.

2.2 Turbulent wake behind a cylinder

In this subsection, we summarize the method and parameters of DNS of turbulent wake behind a circular cylinder. The data examined here is the same as the one used by Fujino et al (2023), which was obtained by DNS using the following method. In this DNS, we solve the Navier–Stokes equations (20) and continuity equation (21) under the boundary conditions shown in Fig. 2(a); namely, we set the uniform flow $U_\infty \boldsymbol{e}_x$ at the inlet and impose the convective condition,

$$\frac{\partial \boldsymbol{u}}{\partial t} + U_m \frac{\partial \boldsymbol{u}}{\partial x} = \boldsymbol{0}\,, \tag{32}$$

at the outlet. Here, U_m denotes the mean convective velocity at the outlet, which we determine by the method proposed by Simens et al (2009) so that the mass conservation is globally ensured. We impose the periodic boundary condition for the other two directions.

Since the streamwise direction is not periodic, we do not use the Fourier spectral method shown in the previous subsection. Instead, we adopt standard finite difference method. More concretely, we evaluate spatial derivatives by the second-order finite difference. One of the difficulties in the DNS of incompressible flow is to conduct temporal integration with accurately satisfying the continuity equation (21). In the present study, we use the Simplified Marker and Cell (SMAC) method (Kajishima and Taira, 2017, § 3.3.2) to achieve this; we use the first-order Euler method for the pressure term the second-order Adams–Bashforth method for the convection term,

and the second-order Crank–Nicolson method for the viscous term to integrate the Navier–Stokes equations by the following four steps:

$$\boldsymbol{u}^P - \Delta t\frac{\nu}{2}\nabla^2\boldsymbol{u}^P = \boldsymbol{u}^n + \Delta t\left(-\nabla P^{n+1} - \frac{3(\boldsymbol{u}\cdot\boldsymbol{\nabla}\boldsymbol{u})^n - (\boldsymbol{u}\cdot\boldsymbol{\nabla}\boldsymbol{u})^{n-1}}{2} + \frac{\nu}{2}\nabla^2\boldsymbol{u}^n\right), \tag{33}$$

$$\nabla^2\phi = \frac{\boldsymbol{\nabla}\cdot\boldsymbol{u}^P}{\Delta t}, \tag{34}$$

$$\boldsymbol{u}^{n+1} = \boldsymbol{u}^P - \Delta t\boldsymbol{\nabla}\phi, \tag{35}$$

$$P^{n+1} = P^n + \phi - \frac{\nu}{2}\Delta t\nabla^2\phi. \tag{36}$$

Here, $P = p/\rho_f$, Δt denotes the time increment, superscript n indicates the value at the n-th time step, and $\boldsymbol{u}^P$ and ϕ are the velocity at the prediction step and correctional pressure. Since when we eliminate ϕ, $\boldsymbol{u}^P$ and P^{n+1} from (33)–(36) we obtain the discrete form of the Navier–Stokes equation (20) and continuity equation (21), we may integrate the velocity field which satisfies (21). Incidentally, we use FFT for the two periodic directions when we solve the Poisson equation (34) for ϕ so that we can employ the direct method. We use the immersed boundary method (Uhlmann, 2005; Kempe and Fröhlich, 2012) to impose the nonslip boundary condition on the cylinder surface. We have validated the DNS by the Strouhal number of the shedding vortices and the mean flow profile (Fujino et al, 2023).

We use the uniform staggered grid (Kajishima and Taira, 2017, § 3.4). Using $8192\times 2560\times 1024$ grid points, we simulate turbulence at the Reynolds number (11), which is defined by the upstream uniform flow velocity U_∞ and the cylinder diameter D, equal to 5000. We have confirmed that the grid spacing is always smaller than 2.6η implying that the smallest eddies are well resolved. On the other hand, the diameter D, which corresponds to the size of the largest eddies, is 128 times larger than the grid width. We expect therefore the existence of hierarchy of vortices with various sizes in the simulated turbulence.

To evaluate the degree of the development of the simulated turbulence, we estimate the Taylor-length Reynolds number (7), which is averaged over the axial direction, as a function of the streamwise position along the center-line. Here, the Taylor length λ was evaluated by

$$\lambda = \sqrt{\frac{\overline{\widetilde{u}_z^2}}{\overline{(\partial\widetilde{u}_z/\partial z)^2}}}, \tag{37}$$

where z is the axial coordinate [Fig. 2(a)] and $\widetilde{\boldsymbol{u}}$ denotes the velocity fluctuation. Thus evaluated Re_λ is shown by open circles in Fig. 3. We can see that Re_λ is about 100, which just satisfies the criterion (10) of developed turbulence.

We also show the one-dimensional longitudinal energy spectrum $E_\parallel$, which is estimated by the Fourier transform in the axial direction of the axial component of fluctuating velocity, by open circles in Fig. 1. Although the wavenumber range is limited because of the smallness of the Reynolds number ($Re_\lambda \approx 100$), we may observe

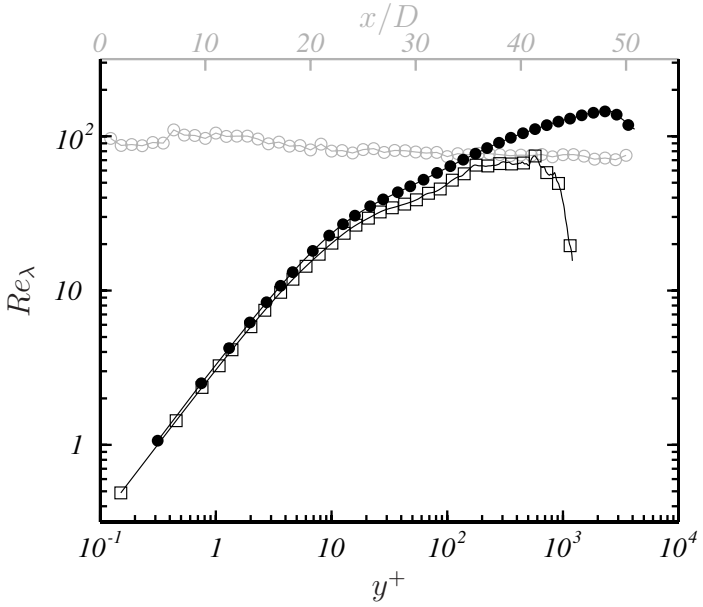

Fig. 3 Spatial distribution of Taylor-length Reynolds number (7) in turbulent wake behind a cylinder (◯), turbulent channel flow (●), and turbulent boundary layer (□). For the turbulent wake, we plot the value averaged in the axial (z) direction as a function of the streamwise location x. For the channel flow, we plot the value averaged in the spanwise (z) and streamwise (x) directions as a function of the distance y from the wall. For the boundary layer, we plot the value average in the spanwise (z) direction as a function of the distance y from the wall, at the streamwise location corresponding to $Re_\theta = 3600$.

power-law spectrum which is consistent with the Kolmogorov similarity (31). Incidentally, we have estimated the mean energy dissipation rate $\bar{\epsilon}$ by $2\nu\overline{\widetilde{S}_{ij}\widetilde{S}_{ij}}$ with $\widetilde{S}_{ij}$ being the rate-of-strain tensor of the fluctuation velocity.

It is also interesting to observe in Fig. 1 that all the energy spectra of the periodic turbulence (solid lines), turbulent wake (open circles), turbulent channel flow (closed circles) and turbulent boundary layer (squares) collapse onto a single universal function in the dissipation range ($k \gtrsim 0.1\eta^{-1}$), if they are normalized by using the mean dissipation rate $\bar{\epsilon}$ and kinematic viscosity ν of each flow. This collapse supports of Kolmogorov (1941)'s similarity hypothesis.

2.3 Turbulent channel flow

Next, in this subsection, we describe the method and parameters of DNS of turbulent channel flow [Fig. 2(b)]. We impose the nonslip boundary condition on the two parallel plane walls, and periodic boundary condition in the other two (spanwise and streamwise) directions. The flow is driven by uniform and steady streamwise external force, and therefore the flow rate fluctuates in time.

The data of turbulent channel flow analyzed in the present article was obtained by the DNS conducted by Lozano-Durán and Jiménez (2014). They conducted the DNS using the method proposed by Kim et al (1987). More concretely, they first rewrite

the Navier–Stokes equation (20) and the continuity equation (21) as the governing equations [Eqs. (3) and (4) in Kim et al (1987)] for the wall-normal components u_y and ω_y of the velocity and vorticity. Then, they numerically integrated these governing equations by the third-order semi-implicit Runge–Kutta method. The spatial derivatives are evaluated by the combination of the Fourier spectral method in the streamwise and spanwise directions and the finite difference method, more precisely a seven-point compact finite difference (Lele, 1992) in the wall-normal direction.

In the present article, we show the analysis of the DNS data with 3072^2 Fourier modes, which correspond to 2048^2 effective modes under the de-aliasing with the 2/3 rule, and the 1081 grid points in the wall-normal direction (i.e. y direction). The grid width in the y direction is non-uniform, which is determined so that the eddies of the Kolmogorov length $\eta(y)$ at the distance y from a wall are well resolved. Recall that, as was estimated in (18) in § 1, $\eta^+ \sim (\kappa y^+)^{\frac{1}{4}}$. We verify this estimation in Fig. 4. Then, according to (18), the grid width in y direction was determined. Thus, the grid widths normalized by the friction length ℓ_τ in each direction are $\Delta x^+ = 12.8$, $\Delta z^+ = 6.4$, $\Delta y^+ = 0.314$–10.7. In the center (i.e. $y = h$) of the channel, $\Delta y/\eta = 1.38$. This implies that even the smallest eddies are well resolved.

The friction Reynolds number (14) of thus simulated turbulence is $Re_\tau = 4179$, which is high enough to investigate hierarchy of vortices. To quantify the development of the turbulence, we estimate Taylor-length Reynolds number (7) averaged over the streamwise and spanwise directions. We show the results by closed circles in Fig. 3 as a function of the distance from the wall. R_λ is about 110 at $y^+ = 630 \approx 0.15h^+$, i.e. at the upper bound of the logarithmic layer (16), and about 145 at $y^+ \approx 2400$, i.e. in the core region in the channel. Therefore, according to the criterion (10), this turbulence is well developed. To further verify the development, we plot the one-dimensional longitudinal energy spectrum $E_\parallel$ at $y^+ = 630$ by closed circles in Fig. 1. Here, the spectrum is estimated by the spanwise Fourier transform of $\widetilde{u}_z$. We observe the power-law scaling (2) in the energy spectrum, $E_\parallel$, of this turbulence.

2.4 Turbulent boundary layer

In this subsection, we describe the method of DNS of turbulent boundary layer developing on a flat plane. Here, we examine the case that flow is uniform $U_\infty \boldsymbol{e}_x$ without pressure gradient in the region sufficiently apart from the plane. The data analyzed in the present study is the same as the one used by Motoori and Goto (2020). This data was obtained by the method similar to the DNS of turbulent wake shown in § 2.2. However, we directly impose the nonslip boundary condition on the plane without using the immersed boundary method.

As shown in Fig. 2(c), in order to save numerical cost, we conduct two separate DNS for upstream and downstream regions. We impose the Blasius laminar solution as the inlet condition of the upstream DNS. Using the tripping forcing proposed by Eitel-Amor et al (2015), we trigger transition to turbulence in the upstream DNS. Then, we save the time-series data of turbulent velocity at the streamwise location corresponding to $Re_\theta = 994$, which we use the inlet condition of the downstream DNS.

The number of grid points in the downstream main DNS is $8064 \times 640 \times 768$. The resolution at the outlet, that is, the location with the most developed turbulence is

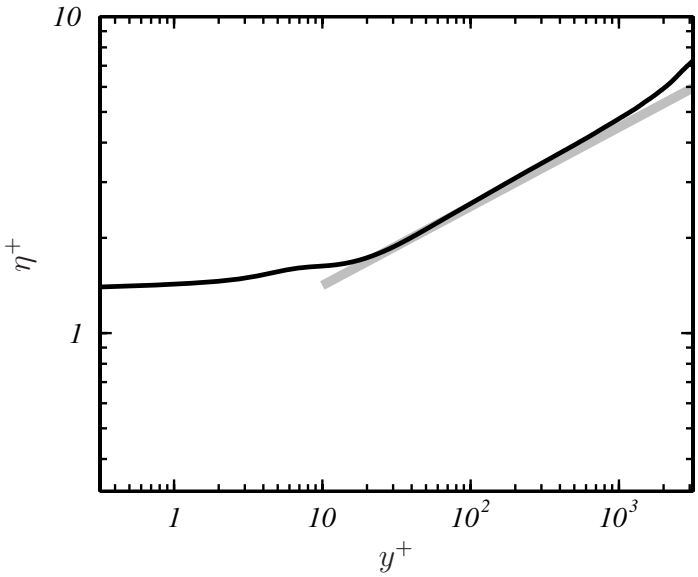

Fig. 4 Kolmogorov length η^+, normalized by the friction length ℓ_τ as a function of the distance $y^+ = y/\ell_\tau$ from the wall in the turbulent channel flow. Gray line indicates $\eta^+ = (\kappa y^+)^{\frac{1}{4}}$ with $\kappa = 0.4$.

$\Delta_x^+ = 10$, $\Delta_z^+ = 5.2$, and $\Delta y^+_{\rm min} = 0.29$ Note that we use non-uniform grid in the y direction. These grid widths are fine enough to resolve the smallest eddies. In fact, $\Delta y/\eta = 1.5$ at $y = \theta/\delta_{99}$. Here, δ_{99} is the boundary layer thickness at which the mean streamwise velocity is equal to $0.99U_\infty$.

By using a large number (about 4×10^9) of grid points and the combination of two DNS, we can simulate turbulence at the Reynolds number (19), defined by the momentum thickness, to be $400 \lesssim Re_\theta \lesssim 4600$, which correspond to $180 \lesssim Re_\tau \lesssim 1380$. To evaluate the degree of development of turbulence, we estimate the Taylor-length Reynolds number (7) at the streamwise direction corresponding to $Re_\theta = 3600$, where the outlet condition is less effective. We show the results by squares in Fig. 3. In this figure, we see that $Re_\lambda \lesssim 75$ at $y^+ \approx 500$ in the most developed region. Although, according to the criterion (10) by Dimotakis (2000), this is not fully developed turbulence, as will be shown in the following sections (see Fig. 14 in § 4.4), we may observe apparent scale separation between the largest and smallest (i.e. Kolmogorov-scale) eddies. In fact, we estimate the one-dimensional longitudinal energy spectrum $E_\parallel$ for $\widetilde{u}_z$ to show results by squares in Fig. 1 for the location at Re_θ =3600 and $y^+ = 165 \approx 1.18\theta^+$. Though we do not observe any scaling range because of the smallness of Re_λ, we do observe a broad spectrum. Thus, we expect a hierarchy of vortices, though they are not self-similar.

3 Forest of small-scale eddies

Let us visualize vortices in turbulence simulated by the methods described in the previous section. Various kinds of vortex identification methods were proposed, and

many of them are based on the velocity gradient tensor,

$$V_{ij} = \frac{\partial u_i}{\partial x_j} \,. \tag{38}$$

Here, we decompose this tensor into the symmetric part $S_{ij} = (V_{ij} + V_{ji})/2$, i.e. the rate-of-strain tensor, and the anti-symmetric part $\Omega_{ij} = (V_{ij} - V_{ji})/2$, i.e. vorticity tensor,

$$\boldsymbol{\Omega} = \frac{1}{2} \begin{pmatrix} 0 & -\omega_3 & \omega_2 \\ \omega_3 & 0 & -\omega_1 \\ -\omega_2 & \omega_1 & 0 \end{pmatrix} \,, \tag{39}$$

where $\boldsymbol{\omega}$ is the vorticity (23). We often use the isosurface of the enstrophy,

$$e = |\boldsymbol{\omega}|^2 \,, \tag{40}$$

or the second invariant,

$$Q = \left(\Omega_{ij}\Omega_{ij} - S_{ij}S_{ij}\right)/2 \,, \tag{41}$$

of the velocity gradient tensor to visualize vortices.

We show in Fig. 5 results of such visualizations. Figs. 5(a) and (b) show the vortices identified by isosurfaces of enstrophy (40) in turbulence in a periodic cube driven by the Taylor–Green forcing (26) and the isotropic forcing (27), respectively. We also visualize vortices in other turbulence by using the second invariant (41) of V_{ij}. Figs. 5(c), (d), and (e) show results for turbulent wake behind the cylinder, turbulent channel flow, and turbulent boundary layer, respectively. Concerning the turbulent boundary layer, Fig. 5(e-i) shows the upstream region ($Re_\theta \approx 180$), whereas Fig. 5(e-ii) visualizes the downstream region ($Re_\theta \approx 3200$–3800).

It is evident in Fig. 5 that we observe a forest of small eddies in all the cases. In other words, we only observe the forest of fine-scale structures, and it is difficult to capture the hierarchy of vortices of different sizes. Recall that Figs. 5(a) and (b) show turbulence with sufficiently high Reynolds numbers, $Re_\lambda = 250$ and 320, respectively. However, even if we magnify the visualizations, Figs. 5(a-ii) and (b-ii), we only observe complex tubular structures, which are sometimes called worms. These worm-like structures have diameters of about 10η and length much longer than η. Though we observe apparent inhomogeneous spatial distribution of these fine-scale structures, which is indeed evidence of spatial intermittency (Frisch, 1995, § 8), we must emphasize that, as will be discussed in the next section, the cluster of fine-scale structures do *not* correspond to larger-sale eddies. Looking at the forest of fine-scale eddies in turbulent wake [Fig. 5(c)], although we may imagine that these small eddies exist around the shedding vortices, we cannot describe the hierarchy of vortices only from this visualization. This observation is similar to the case of turbulent channel flow [Fig. 5(d)], where we only observe small-scale eddies. As for the turbulent boundary layer, we notice interesting phenomena. In the upstream region [Fig. 5(e-i)], vortices triggered by the forcing (Eitel-Amor et al, 2015) are hairpin vortices. Such hairpin-shaped vortices are not artificial due to the specific tripping, but also observed in many experiments (Kline et al, 1967, e.g.). In contrast, in the visualization in the logarithmic and outer layer

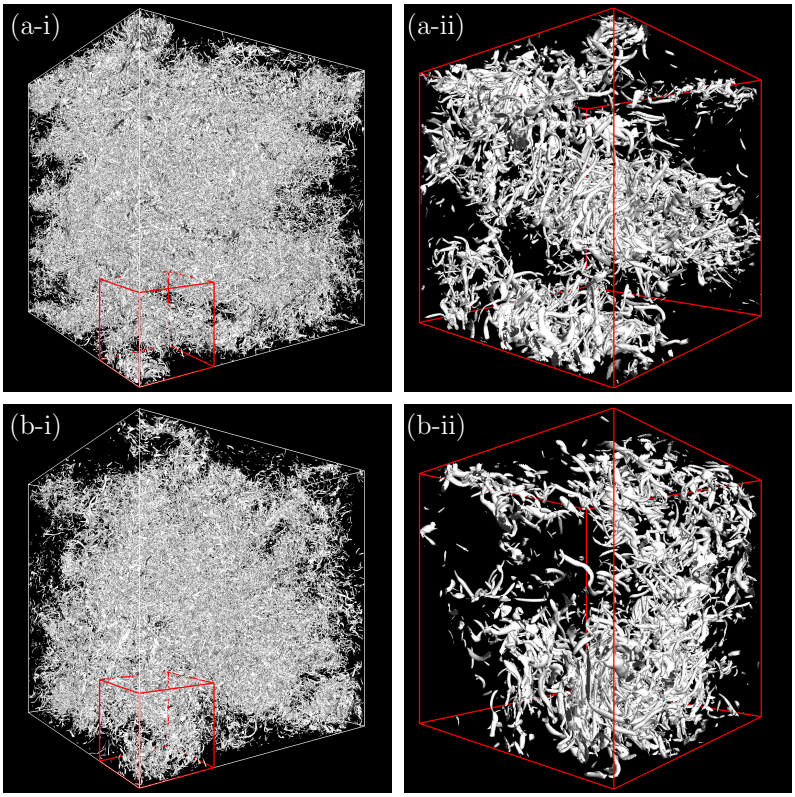

Fig. 5 Forest of smallest-scale vortices in turbulence identified by the isosurface of enstrophy (a, b) or the second invariant of the velocity gradient tensor (c–e). (a) Turbulence in a periodic cube driven by the Taylor–Green force (26). (a-i) shows the entire computational domain; whereas (a-ii) is the magnification of a sub-domain shown in (a-i) with the red lines. (b) Turbulence in a periodic cube driven by the force (27). Similarly to (a), (b-i) shows the entire domain, and (b-ii) is the magnification of a sub-domain. (c) Turbulent wake behind a cylinder. (d) Turbulent channel flow. We show full domain in the streamwise direction and the half domain in the spanwise and wall-normal directions.(e-i) An upstream region ($Re_\theta \approx 180$)and (e-ii) downstream regions ($Re_\theta \approx 3200$–3800) of the turbulent boundary layer.

in the downstream region [Fig. 5(e-ii)], we only observe, similarly to the other turbulence, fine-scale structures. In other words, we cannot identify large-scale structures of the boundary layer only from this visualization [Fig. 5(e-ii)].

As observed in Fig. 5, irrespective of the kind of turbulence, we can only identify smallest scale vortices by the quantities, such as the enstrophy (40) or the second invariant (41), related to the velocity gradient. We may explain this observation as follows. First, recall that the energy spectrum of the developed turbulence is expressed as (2) in the inertial range (3), i.e. $2\pi/L \ll k \ll 2\pi/\eta$. Therefore, the enstrophy spectrum $E_\omega(k)$ is expressed as

$$E_\omega(k) = k^2\, E(k) = C\, \bar{\epsilon}^{\frac{2}{3}}\, k^{\frac{1}{3}} \tag{42}$$

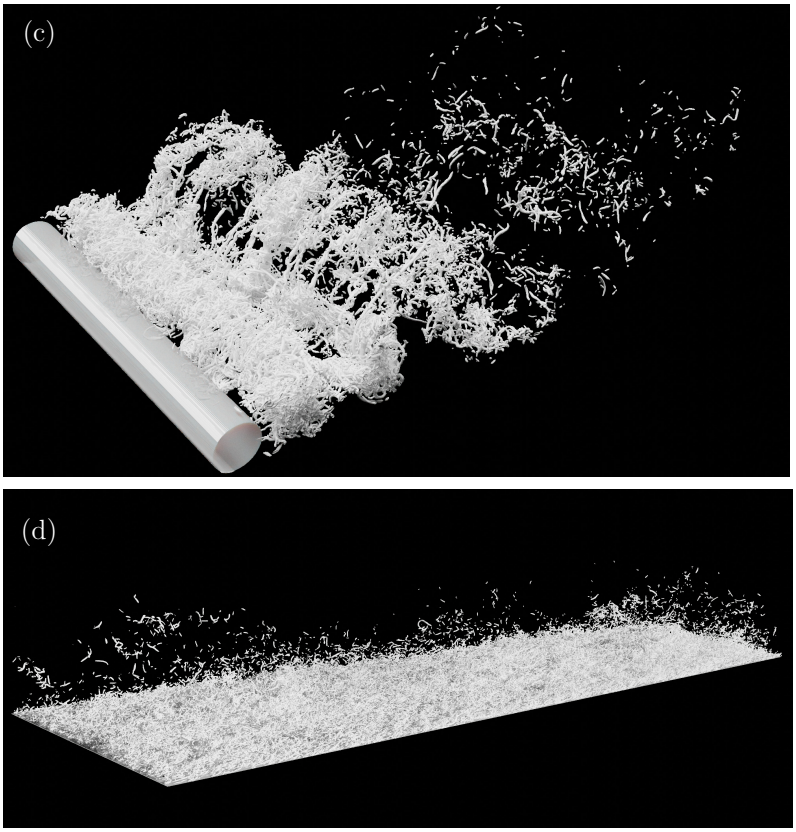

Fig. 5 (continued.)

in the range. Then, the spatial average $\overline{K}$ of the turbulent energy is estimated by

$$\overline{K} = \int_0^\infty E(k)dk \approx \int_{2\pi/L}^{2\pi/\eta} E(k)dk = \frac{3C}{2}\,\overline{\epsilon}^{\frac{2}{3}}\,\left(\frac{L}{2\pi}\right)^{\frac{2}{3}}\,\left[1-\left(\frac{\eta}{L}\right)^{\frac{2}{3}}\right] \sim \overline{\epsilon}^{\frac{2}{3}}\,L^{\frac{2}{3}}\,, \quad (43)$$

which implies that the energy is determined by the largest-scale (i.e. L) vortices. In the above estimation, we have assumed that $L \gg \eta$ because the Reynolds number is sufficiently high; see (6). In contrast, the spatial average $\overline{e}$ of the enstrophy may be estimated by

$$\overline{e} = \int_0^\infty E_\omega(k)dk \approx \int_{2\pi/L}^{2\pi/\eta} E_\omega(k)dk = \frac{3C}{4}\,\overline{\epsilon}^{\frac{2}{3}}\,\left(\frac{\eta}{2\pi}\right)^{-\frac{4}{3}}\,\left[1-\left(\frac{\eta}{L}\right)^{\frac{4}{3}}\right] \sim \overline{\epsilon}^{\frac{2}{3}}\,\eta^{-\frac{4}{3}}\,, \quad (44)$$

which implies that the smallest-scale (i.e. η) vortices are relevant to determine $\overline{e}$ [2]. Therefore, the enstrophy, and velocity gradient, are predominantly determined by

[2] Incidentally, since the spatial average $\overline{\epsilon}$ of the energy dissipation rate is equal to $\nu\overline{e}$, (44) is consistent with the definition (4) of the Kolmogorov length.

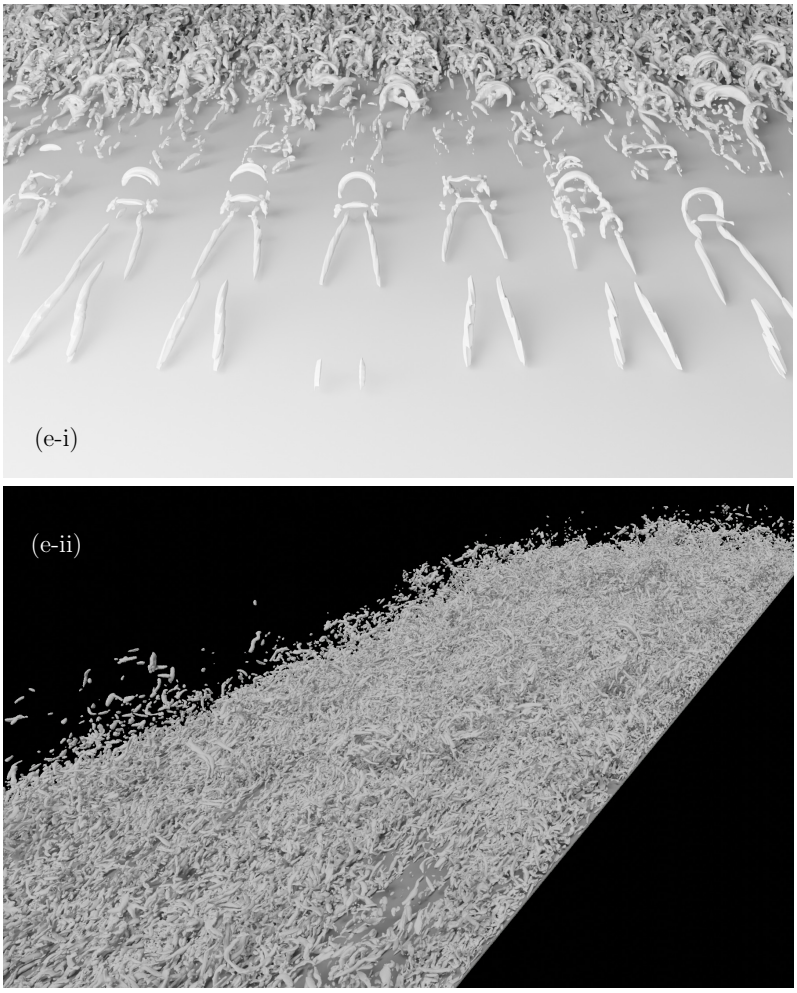

Fig. 5 (continued.)

the smallest eddies. This feature is essential to investigate the hierarchy of vortices in developed turbulence. To conclude, the isosurface of the velocity-gradient related quantities, namely, the enstrophy (40) or the second invariant (41) of the tensor, only capture the smallest vortices.

Since the $-5/3$ power law (2) of the energy spectrum is universal, the above feature is also independent of the kind of turbulence. Therefore, when we use velocity gradient to identify vortices, we always observe only smallest-scale structures. Thus, we need an additional procedure to capture the hierarchy of vortices which must exist in developed turbulence with a broad energy spectrum. In the next section, we can easily achieve this by introducing a scale decomposition.

4 Hierarchy of coherent vortices

As was demonstrated in the previous section, isosurfaces of the enstrophy (40), Figs. 5(a, b), or of the second invariant (41) of the velocity gradient tensor, Figs. 5(c–e), only identify smallest vortices. Therefore, we need one more step to identify the hierarchy of vortices with different sizes in turbulence.

This step is made by the coarse-graining or scale decomposition. In particular, the former was often employed in turbulence research because it is fundamental concept for the LES and extensively investigated since the seminal study by Borue and Orszag (1998). In fact, apart from our studies (Goto, 2008, 2012; Goto et al, 2017; Motoori and Goto, 2019, 2020, 2021; Fujino et al, 2023), there are many other studies (Leung et al, 2012; Cardesa et al, 2017; Doan et al, 2018; Lee et al, 2014; Hwang et al, 2016; Lee et al, 2017; Lozano-Durán et al, 2016, e.g.). in which coarse-graining or scale decomposition are used to investigate flow structures. In the following subsections, we demonstrate that scale decomposition is simple but powerful to identify vortical structures at different scales.

4.1 Turbulence in a periodic cube

In this subsection, we investigate turbulence in a periodic cube. It is easy to implement the coarse-graining by using Fourier transform. More concretely, the low-pass filtering with the cut-off wavenumber,

$$k_c = 2\pi/\sigma \,, \tag{45}$$

corresponds to the coarse-graining at the scale σ. According to an argument similar to the one leading to (44), we can see that thus coarse-grained enstrophy is predominantly determined by flow structures at the scale σ. In fact, such a low-pass filter can capture the hierarchy of vortices with different scales (Goto, 2008; Motoori and Goto, 2019). However, the kinetic energy in the low-pass filtered velocity field is still determined by the integral length, rather than the coarse-graining scale. Therefore, to identify flow structures at scale σ, it is more appropriate to introduce a scale decomposition by using the band-pass filter, which is defined as

$$\widehat{\boldsymbol{u}}_c^{(k_c)}(\boldsymbol{k},t) = \begin{cases} \widehat{\boldsymbol{u}}(\boldsymbol{k},t) & \text{if} \quad |\boldsymbol{k}| \in [k_c/\sqrt{2}, \sqrt{2}k_c) \\ \boldsymbol{0} & \text{otherwise} \end{cases} \tag{46}$$

for the Fourier transform $\widehat{u}_i(\boldsymbol{k},t)$ of $u_i(\boldsymbol{x},t)$. The corresponding real-space band-pass velocity field $\boldsymbol{u}_c^{(\sigma)}(\boldsymbol{x},t)$ is obtained by the inverse Fourier transform of $\widehat{\boldsymbol{u}}_c^{(k_c)}(\boldsymbol{k})$. This procedure is known also as Littlewood–Paley decomposition.

We then define the scale-decomposed vorticity as $\boldsymbol{\omega}_c^{(\sigma)} = \boldsymbol{\nabla} \times \boldsymbol{u}_c^{(\sigma)}$ to estimate the enstrophy $|\boldsymbol{\omega}_c^{(\sigma)}|^2$ at each scale σ. Isosurfaces of this quantity are shown in Fig. 6. In these figures, the red objects are vortices at the scale of the forcing, i.e. $\sigma = 1600\eta$ [Fig. 6(a)] for the Taylor–Green forcing (26) and $\sigma = 1500\eta$ [Fig. 6(b)] for the forcing (27). Yellow and blue objects are isosurfaces of enstrophy decomposed at the 1/4 and 1/16 scales, respectively. Incidentally, the reason why we have chosen the scales with

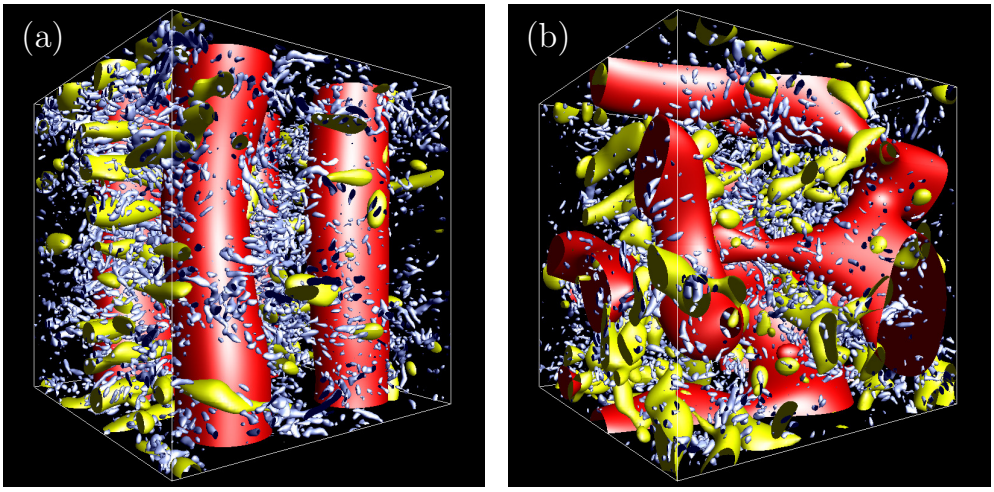

Fig. 6 Scale-decomposed vortical structures in turbulence in a periodic cube driven by (a) the Taylor–Green force (26) and (b) the homogeneous isotropic force (27). Red, blue, and yellow vortices are visualized by isosurface of enstrophy (40) scale-decomposed at (a) $\sigma = 2\pi/k_c = 1600\eta$, 400η, and 100η, and at (b) 1500η, 360η, and 90η, respectively. We visualize the entire cubic domain of size (a) $(2200\eta)^3$ and (b) $(2100\eta)^3$.

factor 1/4 is that vortices tend to align to the most extensional direction of the rate-of-strain tensor on the 3–5 times larger scale (Leung et al, 2012). We can see that there exist coherent vortices at each scale, even for scales much larger than the Kolmogorov length η in both turbulence. It is difficult to observe relations between vortices at different scales only from the global visualization (Fig. 6). However, as shown in the following, vortices in successive length scales do have characteristic correlations.

First, let us examine, in detail, the hierarchy (Fig. 7) of vortices in turbulence driven by the Taylor–Green forcing (26). As shown in Fig. 7(a), the largest vortices (the red objects at $\sigma = 1600\eta$) are those directly sustained by the force (26). Though we cannot see these four columns in the visualization [Fig. 5(a)] of the raw enstrophy without the scale decomposition, they do exist in the turbulence. It is further interesting to observe the next generation of coherent vortices (yellow objects at $\sigma = 400\eta$) around these red vortices [Fig. 7(a)]. In this figure, we visualize the yellow vortices only in the domain denoted by the yellow dashed lines, where four conspicuous vortex tubes exist. Note that their axis is parallel to the stretching direction in the velocity field induced by the red vortices [see also Fig. 3 of Goto et al (2017)]. This means that yellow vortices at scale 400η are stretched and amplified by the strain rate around the red ones at 1600η. We also observe that the yellow vortices tend to form the counter-rotating pairs. This tendency can be quantitatively verified in turbulence in a periodic cube irrespective of forcing (Goto et al, 2017, Fig. 8).

Fig. 7(b) shows a magnification of the subdomain indicated by the solid yellow lines in Fig. 7(a). We may observe the relationship between them and smaller (blue) vortices at scale 100η. Since there exist strain-rate field around the pair of yellow vortices, the smaller blue vortices are stretched and amplified by the strain-rate field. This explains the observation that blue vortices are perpendicular to the yellow ones.

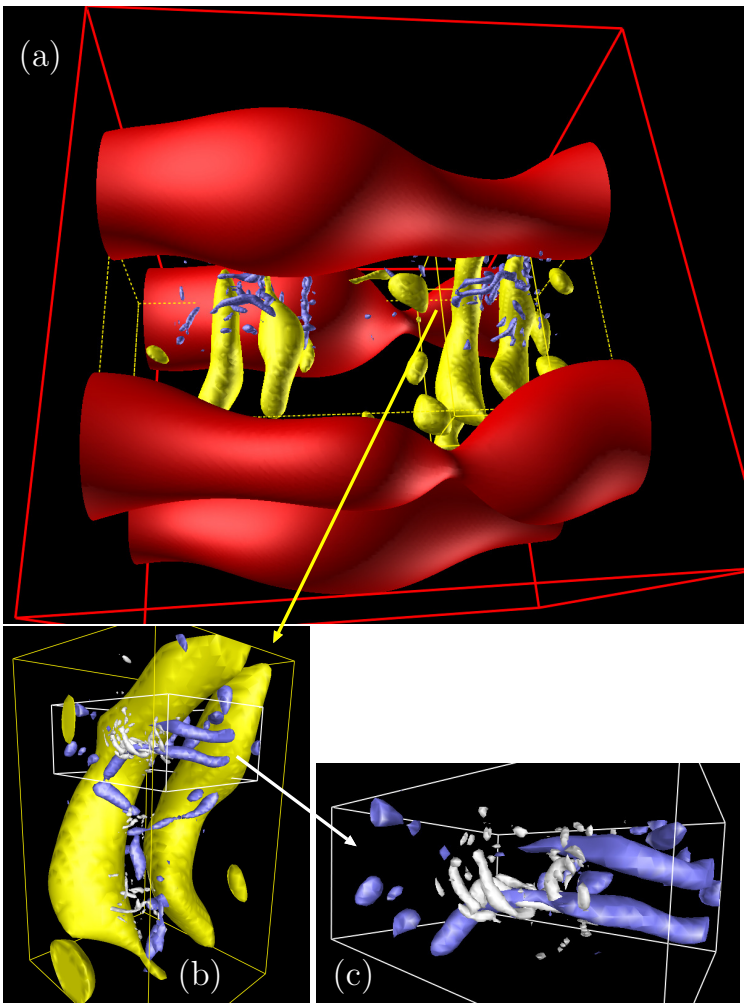

Fig. 7 Hierarchy of vortices in turbulence driven by Taylor–Green force (26). Red, yellow, blue, and white objects are vortices identified by isosurface of enstrophy scale-decomposed at $\sigma = 2\pi/k_c = 1600\eta$, 400η, 100η, and 25η, respectively. (a) We visualize red vortices in the entire computational domain of size $(2200\eta)^3$ and yellow vortices in a subdomain $(770\eta \times 900\eta \times 2200\eta)$ indicated by the yellow dashed lines. (b) Magnified view of the subdomain $(540\eta \times 900\eta \times 490\eta)$ indicated by the yellow solid lines in (a). (c) Magnified view of the subdomain $(440\eta \times 190\eta \times 340\eta)$ indicated by the white solid lines in (b).

It is also interesting to observe that two counter-rotating blue vortices form a pair. Fig. 7(c) is a magnification of the field around this counter-rotating pair. We may observe further smaller (white) vortices at scale $\sigma = 25\eta$ are, again, stretched and amplified in the strain-rate field around the pair of blue vortices. Moreover, we observe that the white vortices also form a counter-rotating pair. Therefore, they would stretch and amplify further smaller vortices in the strain-rate field around them. However, as discussed in the next paragraph, since at their scale ($\sigma = 25\eta$) the viscous effects

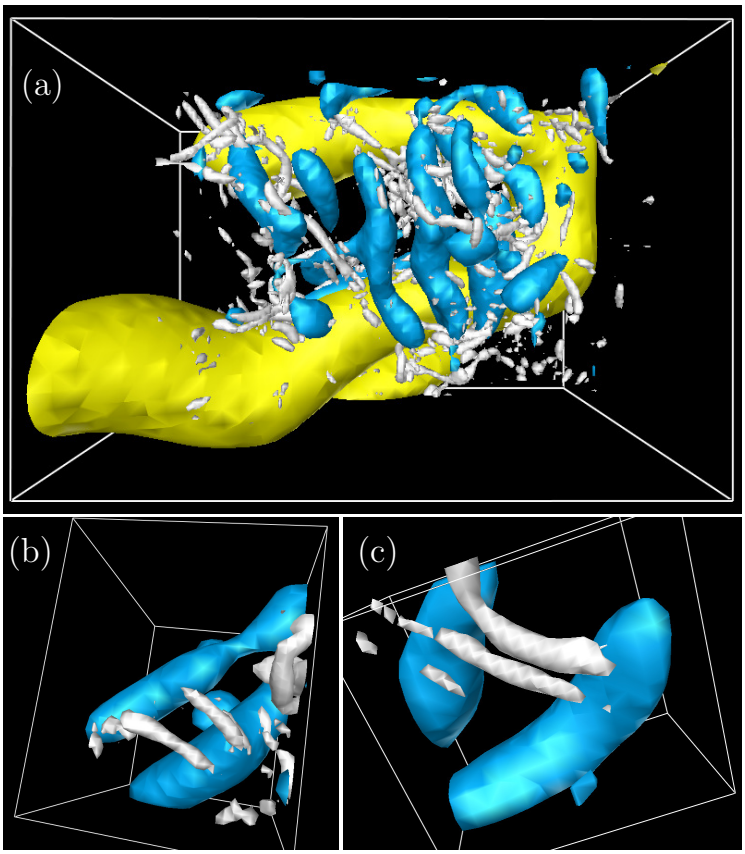

Fig. 8 Hierarchy of vortices in turbulence driven by the homogeneous isotropic force (27). Yellow, blue, and white objects are vortices identified by isosurface of enstrophy scale-decomposed at $\sigma = 2\pi/k_c = 360\eta$, 90η , and 23η, respectively. We crop the subdomains in the same snapshot of size (a) $590\eta \times 400\eta \times 480\eta$, (b) $120\eta \times 140\eta \times 180\eta$, and (c) $110\eta \times 120\eta \times 80\eta$.

dominate the stretching, the cascading process due to the vortex stretching terminate at this scale in the examined turbulence.

We consider the observed scale-by-scale vortex stretching process in terms of its timescales. According to the argument similar to the one leading to (44), vortices with size σ have enstrophy proportional to $\bar{\epsilon}^{\frac{2}{3}}\sigma^{-\frac{4}{3}}$. This implies that their vorticity and strain rate is scaled as $\bar{\epsilon}^{\frac{1}{3}}\sigma^{-\frac{2}{3}}$. Thus, these vortices can create smaller vortices in the timescale,

$$\tau_s \sim \bar{\epsilon}^{-\frac{1}{3}}\sigma^{\frac{2}{3}} . \tag{47}$$

On the other hand, the viscous timescale of these vortices is

$$\tau_v \sim \frac{\sigma^2}{\nu} \tag{48}$$

Therefore, if $\tau_s \lesssim \tau_v$, they can create smaller vortices by stretching before they die due to the viscosity. In fact, we may show that $\tau_s \sim \tau_v$ for σ comparable with the

Kolmogorov length η, (4), which corresponds to the size of the smallest vortices. We have also quantitatively shown that this scale-by-scale vortex stretching explains the scale-local energy transfer in turbulence (Yoneda et al, 2022, Fig. 1).

Next, let us observe the case (Fig. 8) with the other forcing (27). Similarly to the previous case, we only need to employ the band-pass filter (46) to observe the hierarchy of vortices with different sizes. Recall that though the external force (27) inputs the energy to the system, it does not prescribe coherent structures. This explains the reason why no characteristic flow structures exist at the forcing scale; see the red objects in Fig. 6(b), which are isosurfaces of the enstrophy at the scale $\sigma = 1500\eta$. In contrast, we may observe coherent tubular vortices at smaller scales. We demonstrate this in Fig. 8. Panel (a) of this figure shows a typical example, where the yellow vortices at scale $\sigma = 360\eta$ form a counter-rotating pair. In the figure, we also show smaller vortices: namely, blue vortices at $\sigma = 90\eta$ and white ones at $\sigma = 23\eta$. It is evident that blue vortices are perpendicular to the yellow vortex pair because they align to the stretching direction in the rate-of-strain field at the scale of yellow vortices. We also observe that further smaller vortices, i.e. white objects at $\sigma = 23\eta$, are cratered around the blue vortices. Moreover, we may easily find many examples [Figs. 8(b, c)] of counter-rotating pairs of blue vortices ($\sigma = 90\eta$) in the same snapshot and the creation of smaller white vortices ($\sigma = 23\eta$) around them. In contrast to the case (Fig. 7) with the Taylor–Green forcing, largest vortices are random in turbulence driven by the homogeneous isotropic force (27). Nevertheless, smaller-scale vortices spontaneously become coherent, and they seem to have common features independent of the forcing.

Since visualizations like Figs. 7 and 8 depend on the isosurface threshold, they have ambiguity. However, the answer to the frequently asked question "Can we observe larger-scale structures if we decrease the threshold for smaller-scale vortices?" is "no". Recall that smaller vortices are created around larger vortices, and therefore we cannot observe larger vortices even for a smaller threshold. In other words, a large vortex is not a cluster of smaller vortices. This can be demonstrated by an objective identification of vortices. Here, we use the low-pressure method (Miura and Kida, 1997; Kida and Miura, 1998) as a threshold-free identification scheme. We extend this method for the scale-decomposed velocity field (Goto et al, 2017) to objectively identify the axis of tubular vortices on each level in the hierarchy. We show thus identified vortex axes in Fig. 9. In this figure, we may see that the vortex axes are space-filling (Tsuruhashi et al, 2022) and a large-scale vortex axis is not a bundle of smaller-scale vortex axes. We also observe that though the characteristics of large-scale vortex axes depend on forcing [Figs. 9(a-i, b-i)], they are similar at smaller scales [Figs. 9(a-iii, b-iii)].

We have explained the creation of smaller-scale eddies (i.e. the energy cascade) in terms of the scale-by-scale vortex stretching. This picture is, in fact, a classical view (Tennekes and Lumley, 1972, § 8.2), and not only ourselves (Goto, 2008, 2012; Goto et al, 2017) but also many other authors (Hussain, 1986; Melander and Hussain, 1993; Leung et al, 2012; Doan et al, 2018, e.g.) discussed the role of vortex stretching in the energy cascade. We must emphasize that we have to look for typical examples such as shown in Figs. 7 and 8 which explain the role of vortex stretching in the cascade. This is because, as shown in Fig. 9, in statistically steady turbulence, vortices at each scale are space-filling and they are sometimes weakened and sometimes strengthened. In

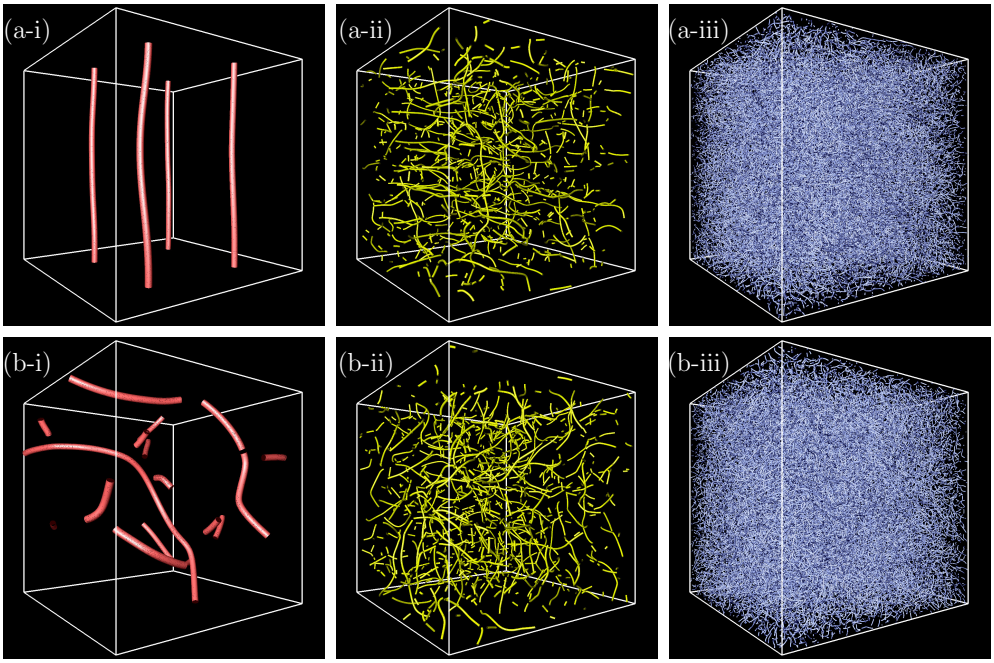

Fig. 9 Hierarchy of vortex axes identified by the extended low-pressure method in turbulence in a periodic cube driven by (a) Taylor–Green force (26) and (b) the homogeneous isotropic force (27). Panels (a) and (b) are the same snapshots as in Fig. 6(a) and Fig. 6(b). The scale of the decomposition is (a-i) 1600η, (a-ii) 400η, (a-iii) 100η, (b-i) 1500η, (b-ii) 360η, and (b-iii) 90η.

other words, vortices at different ages coexist. Therefore, we need to find the moment of the birth of smaller vortices to show clear examples such as Figs. 7 and 8. This is not the case in evolving flow. We may easily observe events of smaller vortices creation by vortex stretching in the downstream region (Fig. 11) of turbulent wake behind a cylinder, which is examined in the next subsection, or in turbulent flow created by a collision of two vortex rings (McKeown et al, 2020) because the moment of birth of smaller vortices is apparent in these flows.

4.2 Turbulent wake behind a cylinder

In this subsection, we examine the hierarchy of vortices in turbulent wake behind a circular cylinder. As was demonstrated in Fig. 5(c), we only observe fine vortices when we identify vortices by isosurface of the second invariant (41) of velocity gradient tensor. However, as shown in Fig. 3, Re_λ is about 100, which marginally satisfies the criterion (10) for developed turbulence, and the energy spectrum $E_{\parallel}$ shown in Fig. 1 also exhibits a power law indicating the existence of self-similar hierarchy of vortices. Hence, we introduce a scale decomposition similarly to the case of periodic turbulence examined in the previous subsection. However, since we do not impose a periodic boundary condition in the streamwise direction, we cannot use the Fourier band-pass filter (46) for scale decomposition.

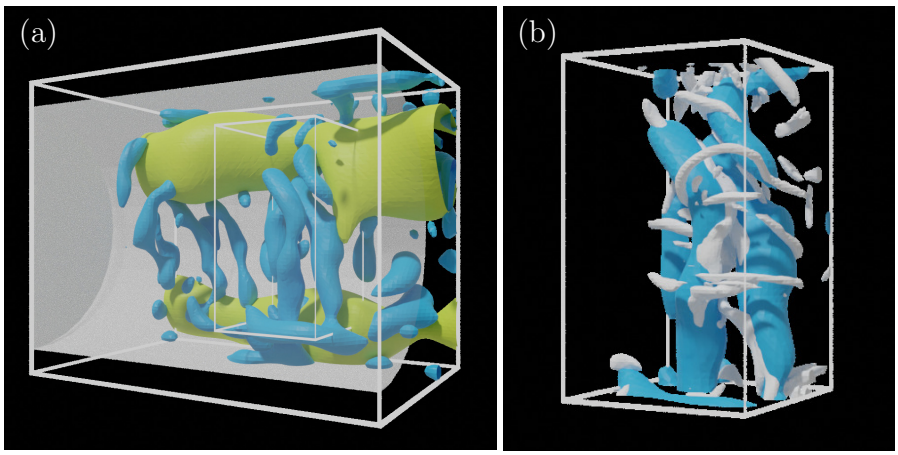

Fig. 10 Hierarchy of vortices in the recirculation region of the turbulent wake behind a cylinder. Yellow and blue objects are vortices identified by isosurface of the second invariant (41) of the velocity gradient tensor scale-decomposed at scale $\sigma = L_*/4$ and $L_*/16$. Here, L_* ($\approx 0.8D$) is defined by (52). (a) Visualization in the domain $0 \le x/D \le 1$, $-0.6 \le y/D \le 0.6$, $0.5 \le z/D \le 2$. The origin is set at the center of the cylinder shown with the white surface. (b) Visualization of the subdomain indicated by white thin lines in (a).

Thus, we introduce a scale-decomposition method in real space. To this, we first define the mean and fluctuation velocities as

$$\boldsymbol{u}(\boldsymbol{x},t) = \overline{\boldsymbol{u}}(\boldsymbol{x}) + \widetilde{\boldsymbol{u}}(\boldsymbol{x},t)\,. \tag{49}$$

Then, we coarse-grain the fluctuating velocity $\widetilde{\boldsymbol{u}}(\boldsymbol{x},t)$ by the Gaussian filter

$$\boldsymbol{u}^{[\sigma]}(\boldsymbol{x},t) = \frac{1}{(\sqrt{2\pi}\sigma)^3}\int \widetilde{\boldsymbol{u}}(\boldsymbol{x}_p,t)\exp\left[-\frac{|\boldsymbol{x}-\boldsymbol{x}_p|^2}{2\sigma^2}\right]\,d\boldsymbol{x}_p \tag{50}$$

at scale σ. Since $\boldsymbol{u}^{[\sigma]}(\boldsymbol{x},t)$ contains the flow information at scales larger than σ, we define

$$\boldsymbol{u}^{(\sigma)}(\boldsymbol{x},t) = \boldsymbol{u}^{[\sigma]}(\boldsymbol{x},t) - \boldsymbol{u}^{[2\sigma]}(\boldsymbol{x},t) \tag{51}$$

which contains flow structures scales between σ and 2σ. We expect thus defined velocity field $\boldsymbol{u}^{(\sigma)}$ has similar property with the one $\boldsymbol{u}_c^{(\sigma)}$ defined by using the Fourier band-pass filter (46).

As discussed by Fujino et al (2023) in detail, the sustaining mechanism of turbulent wake behind a cylinder is different in three distinct regions: namely, the separation shear layer, the recirculation region just behind the cylinder, and the downstream region. Since the hierarchy of vortices in the separation shear layer is not clear at the present Reynolds number ($Re_D = 5000$), in the following, we examine the hierarchy of vortices in the latter two regions.

First, we show in Fig. 10(a) the hierarchy of vortices identified by the scale decomposition by (51). In this figure, yellow and blue objects are isosurfaces of the second

invariant (41) of velocity gradient tensor at the scale $\sigma = L_*/4$ and $\sigma = L_*/16$, respectively. Here,

$$L_* = U_\infty/(2\pi f_*) \tag{52}$$

denotes the scale of the largest vortices (i.e. the shedding vortices identified as red objects in Fig. 11) which is defined in terms of the shedding frequency f_* (Yasuda et al, 2020). Incidentally, we have estimated f_* by the peak of the power spectrum (Fujino et al, 2023, Fig. 2). In this recirculation region, the stationary twin vortices exist, and its fluctuation are captured by the yellow vortices at scale $\sigma = L_*/4$. Since they are a counter-rotating pair, a strain-rate field whose stretching direction is in y direction [see Fig. 2(a)] exists in the region between them and the cylinder. It is this straining field that stretches and amplifies smaller ($\sigma = L_*/16$) blue vortices whose axis is parallel to the y direction. The process that yellow counter-rotating vortices stretch and create smaller blue vortices is similar to those observed in turbulence driven by the Taylor–Green vortices [Fig. 7(a)]. Incidentally, however, we must note that there coexist blue vortices created in the nearby shear layer in the visualization (Fig. 10) as more carefully discussed by Fujino et al (2023). Furthermore, we show in Fig. 10(b) a subdomain of Fig. 10(a) together with the white isosurfaces of the second invariant (41) of velocity gradient tensor without the scale decomposition. It is evident that, due to the stretching in the strain-rate field in front of the blue vortex pair, smaller white vortices are created. This event is also similar to those observed in turbulence in a periodic cube (Figs. 7 and 8).

Next, we examine the hierarchy of vortices in the downstream region of the wake. The hierarchy in this region sufficiently apart from the obstacle is similar to the turbulence in the periodic cube. As discussed in the previous subsection, the creation process of smaller vortices in the periodic turbulence is sometimes unclear because there coexist vortices at different ages in a snapshot. In contrast, since smaller and smaller vortices are created successively in downstream of the wake, the process is rather clear. We show results of the scale decomposition in Fig. 11. We immediately notice that shedding roller vortices, which correspond to the Kármán vortex street, are identified as red objects even in this turbulent regime at $Re_D = 5000$. These red objects are the isosurfaces of the second invariant of the velocity gradient tensor scale-decomposed at $\sigma = L_*$. Even though we observe some smaller-scale yellow and blue vortices inside a roller vortex, its circulation is determined mainly by the largest scale L_*. Since the nearest-neighbor roller vortices are counter-rotating, there exists strain-rate field between them. Therefore, smaller (i.e. $\sigma = L_*/4$) vortices, which are called the rib vortices are stretched, amplified, and created in the strain-rate field [Fig. 11(a)]. We emphasize that there are characteristics in the swirling directions of the created (yellow) rib vortices; namely, they form counter-rotating pairs which induce compression on the side of roller vortices [Fig. 11(b)]. This explains that the (yellow) rib vortices weaken roller vortices (their parents) by vortex compression, whereas they stretch and create smaller (blue, $\sigma = L_*/16$) vortices in the strain-rate field in front of the pairs. In fact, we quantitatively demonstrated that rib vortices compress and weaken roller vortices (Fujino et al, 2023, § 5.5). In summary, in the downstream region of the wake, the energy cascading process starting from the shedding roller vortices sustains the hierarchy of vortices.

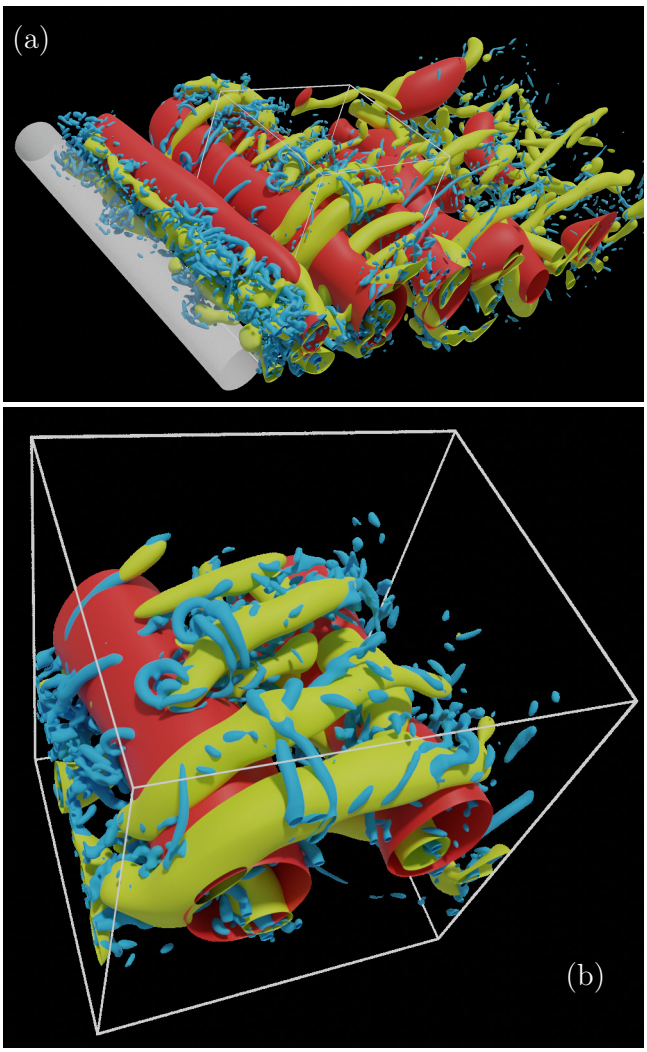

Fig. 11 Hierarchy of vortices at scales $\sigma = L_*$ (red), $\sigma = L_*/4$ (yellow), and $\sigma = L_*/16$ (blue) in the downstream region of turbulent wake behind a cylinder. (a) Visualization in the whole computational domain, which may be compared with the one without the scale decomposition [Fig. 5(c)]. (b) Visualization in the subdomain ($2.8 \le x/D \le 7$, $-2.5 \le y/D \le 2.5$, $2.5 \le z/D \le 6$) indicated by white lines in (a).

4.3 Turbulent channel flow

In this subsection, we consider the hierarchy of vortices (Fig. 12) and its sustaining mechanism in turbulent channel flow. In Fig. 12, red, yellow, and blue objects are vortices identified by the isosurface of the second invariant of the velocity gradient tensor scale-decomposed at $\sigma^+ = 960$, 240, and 60, respectively. We visualize a global field in Fig. 12(a), which shows the entire computation domain in the streamwise direction and the half domain in the spanwise and wall-normal directions. The largest

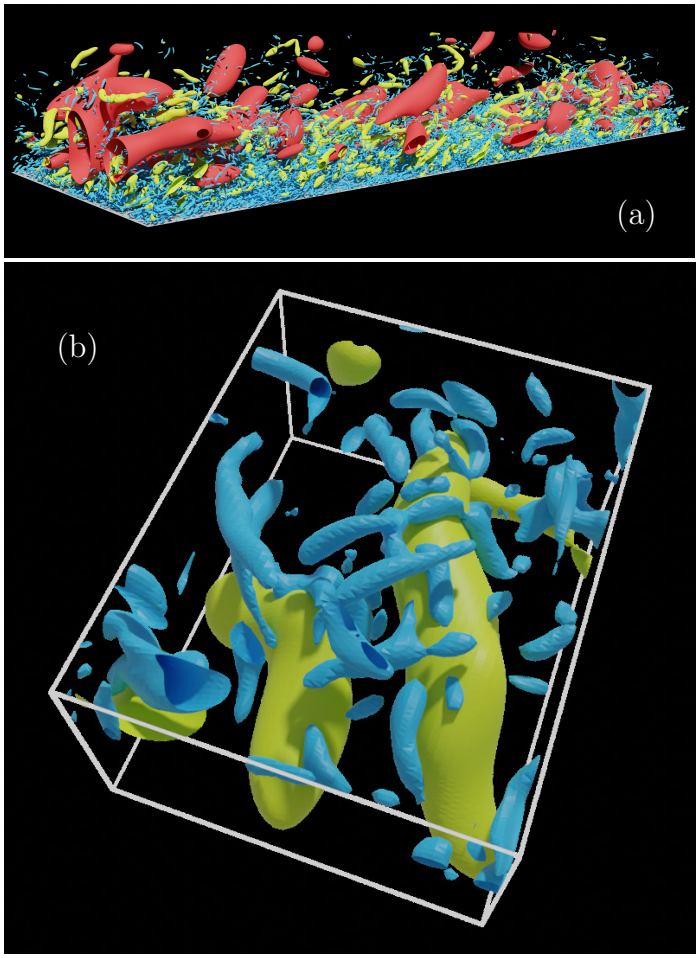

Fig. 12 Hierarchy of coherent vortices in turbulent channel flow. Red, yellow, and blue vortices are identified by the isosurface of the second invariant (41) of velocity gradient tensor scale-decomposed at $\sigma^+ = 960$, 240, and 60. Note that $\sigma^+ = 60$ corresponds to $\sigma/\eta = 10$–20 for $y^+ \gtrsim 100$. Visualizations in (a) the same domain as in Fig. 5(d) and (b) a subdomain at the distance $1230 \le y^+ \le 1920$ from the wall with the streamwise and spanwise size of $\delta x^+ = 1150$ and $\delta z^+ = 1450$.

(red) vortices tend to form a streetwise longitudinal vortex tube. We expect from the energy cascade picture that smaller vortices (say, yellow ones at $\sigma^+ = 240$ and blue ones at $\sigma^+ = 60$) are successively created. Though it is rather difficult to observe such events in the global visualization in Fig. 12(a), we may find examples in a magnified view such as shown in Fig. 12(b). In this panel, we see that (blue) smaller ($\sigma^+ = 60$) vortices are stretched and amplified in the strain-rate field sustained around the counter-rotating pair of (yellow) larger ($\sigma^+ = 240$) vortices. This observation is similar to those in the periodic turbulence (Figs. 7 and 8) and in the turbulent wake (Figs. 10 and 11).

However, since there coexist vortices with different ages in this turbulence [Fig. 12(a)], relations between the two different scales are not always as clear as in Fig. 12(b). This is similar to the observation in the periodic turbulence, and in contrast to the downstream of the turbulent wake (Fig. 11), where smaller vortices are successively created. Nevertheless, we emphasize that we can observe similar events like in Fig. 12(b) for turbulent channel, in Figs. 7(b, c) and Fig. 8 for periodic turbulence, and in Figs. 10(b) and 11(b) for turbulent wake. This may imply the common feature of the sustaining mechanism of small vortices in regions away from solid walls. We also emphasize that the mechanism of energy cascade in terms of vortex stretching is not only based on these visualizations but also on the quantification developed by Yoneda et al (2022, Fig. 1) and Fujino et al (2023, Fig. 10).

It may be obvious that the largest eddies in turbulence in a periodic cube are sustained by external force and those are shedding vortices or stationary twin vortices in turbulent wake behind an obstacle. Then, how are the largest eddies [i.e. red vortices in Fig. 12(a)] sustained in the turbulent channel flow? We must consider this issue depending on the distance y from the wall because, at the distance y, the largest eddies (i.e. wall-attached eddies) have size comparable with y. Then, by a simple quantification in the following, we may show that wall-attached eddies are created by the stretching due to the mean shear flow.

Taking the inner product of the vorticity equation (22) and $\boldsymbol{\omega}$, we see that the production of the enstrophy (41) due to the vortex stretching is expressed as $\omega_i S_{ij} \omega_j$. Then, we consider the contributions to this production rate of enstrophy of vortices with scale σ from two effects. One is the contribution from the twice-larger-scale rate-of-strain $S_{ij}^{(2\sigma)}$, and the other is contribution from the mean flow. Note that the former is contribution of an energy cascading process. Then, we define the ratio,

$$\Gamma(\sigma) = \left\langle \frac{\omega_i^{(\sigma)} S_{ij}^{(2\sigma)} \omega_j^{(\sigma)}}{\omega_i^{(\sigma)} \omega_i^{(\sigma)}} \right\rangle_{xz} \Bigg/ \left\langle \frac{\omega_i^{(\sigma)} \overline{S}_{ij} \omega_j^{(\sigma)}}{\omega_i^{(\sigma)} \omega_i^{(\sigma)}} \right\rangle_{xz} \tag{53}$$

between the two contributions. In (53), $\langle \cdot \rangle_{xz}$ denotes the average over the plane parallel to the wall, $S_{ij}^{(\sigma)}$ is the rate-of-strain tensor estimated from the velocity field $\boldsymbol{u}^{(\sigma)}$ scale-decomposed at σ, and $\overline{S}_{ij} = (\partial \overline{u}_i / \partial x_j + \partial \overline{u}_j / \partial x_i)/2$ is the rate-of-strain tensor of the mean flow $\overline{\boldsymbol{u}}$. We estimate (53) as a function of y and σ and show results in Fig. 13(a).

By definition of Γ, when $\Gamma < 1$, vortices are directly created by the mean flow. In Fig. 13(a), the blue line indicates $\Gamma = 1$. In this figure, the red line denotes the $0.7L_c(y)$, where $L_c(y)$ is the Corrsin length at the distance y from the wall; and the black dotted line denotes $0.7\kappa y$. We can see these three lines coincide in the logarithmic layer. This coincidence can be explained as follows. First, we recall that L_c is defined by the length scale of vortices accompanied with a strain rate comparable with the mean shear rate,

$$\frac{\partial \overline{u}_x}{\partial y} \approx \frac{u_\tau}{\kappa y} \,. \tag{54}$$

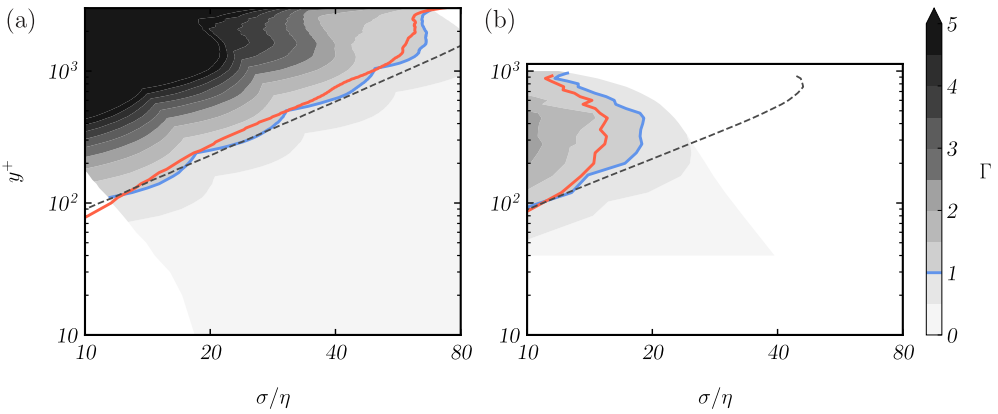

Fig. 13 Ratio Γ defined by (53) of the contributions to the enstrophy production rate at scale σ from the twice larger strain rate $S_{ij}^{(2\sigma)}$ and the mean flow shear $\overline{S}_{ij}$ as a function of the distance y from the wall and σ. Blue, red, and black dotted curves denote $\Gamma = 1$ and $0.7L_c(y)$, and $0.7\kappa y$. Here, $L_c(y)$ is the Corrsin length. (a) Averaged value over the spanwise and streamwise directions in turbulent channel flow. (b) Averaged value in the spanwise direction at the streamwise location corresponding to $Re_\theta = 3600$ in the turbulent boundary layer.

Here, we have used the logarithmic law (15) of the mean flow. Then, since the strain rate around vortices with size ℓ is estimated as

$$\left(\frac{\overline{\epsilon}}{\ell^2}\right)^{\frac{1}{3}} \approx \left(\frac{u_\tau^3}{\kappa y \ell^2}\right)^{\frac{1}{3}} \tag{55}$$

because the mean energy dissipation rate in the logarithmic layer is estimated as (15). Then, requiring that (54) and (55) are balanced at $\ell = L_c$, we obtain $L_c(y) = \kappa y$.

Thus, Fig. 13(a) implies that small vortices (i.e. wall-detached eddies), which satisfy

$$\sigma < L_c(y) \quad (\approx y) \tag{56}$$

are created through energy cascade by being stretched and amplified by larger vortices. On the other hand, larger (i.e. $\sigma > L_c(y) \approx y$) vortices (i.e. wall-attached eddies) are directly created by being stretched by mean shear. Although wall-detached eddies smaller than L_c ($\approx y$) are also stretched by the mean shear, the timescale is slower than the stretching due to larger vortices. This explains the reason why these smaller eddies are created by the energy cascading process.

In summary, at the distance y from a solid wall, eddies larger than L_c ($\approx y$) are directly created by mean-flow stretching, whereas eddies smaller than L_c ($\approx y$) are created in strain-rate field sustained around larger vortices. In other words, in the logarithmic layer (16) of wall turbulence, the largest eddies which acquire energy from the mean flow create smaller vortices through similar process to those in periodic turbulence and downstream of turbulent wake. Fig. 13(a) clearly implies that "in region ($y^+ \gtrsim$ 30–100) away from solid walls, small ($\sigma \lesssim L_c(y)$) vortices are created

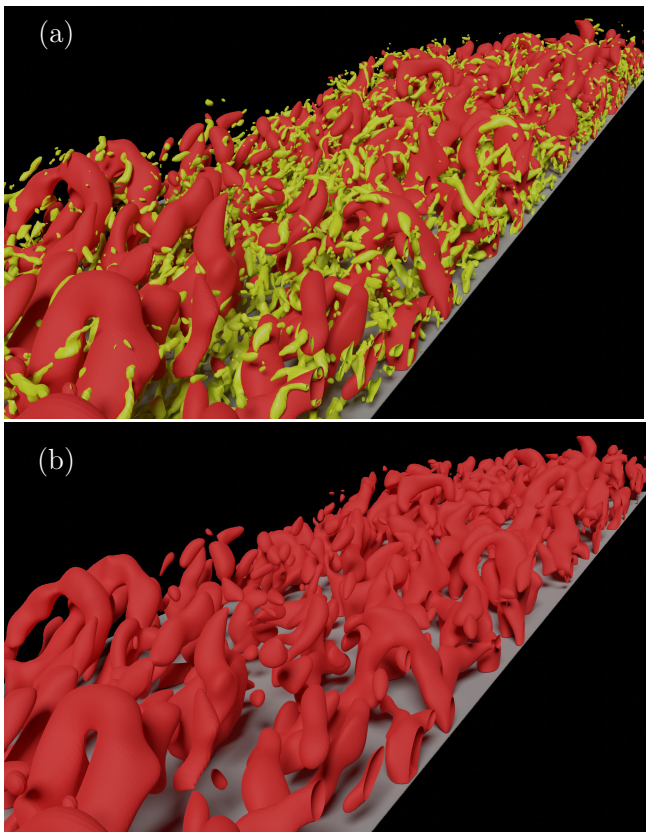

Fig. 14 (a) Coherent vortices in turbulent boundary layer at the location corresponding to $Re_\theta = 3200$–3800. Red and yellow vortices are identified by isosurface of enstrophy at scale $\sigma = 200\ell_\tau \approx 0.18\delta_{99} \approx 1.4\theta$ and $\sigma = 40\ell_\tau$, respectively. (b) Only the large-scale vortices are visualized.

through energy cascade." This is consistent with the Kolmogorov–Richardson view of the energy cascade.

Incidentally, Fig. 13(a) also shows that in the near wall region (i.e. in the buffer layer, $y^+ \lesssim 30$–100), $L_c(y) \lesssim 10\eta$. This implies that there is no hierarchy of vortices in the buffer layer, and the vortices directly interact with mean flow. In fact, it is well-known as the self-sustaining process [SSP, Hamilton et al (1995)] that the single-scale streamwise vortices and streak structures interact each other to sustain themselves in the buffer layer. Therefore, we may speculate that the largest wall-attached eddies at each distance from the wall can be sustained by SSP-like process. In other words, there may exist a hierarchy of SSP [Hwang and Bengana (2016); see also Marusic and Monty (2019, § 4.1)] in the logarithmic layer of wall turbulence at high Reynolds numbers.

4.4 Turbulent boundary layer

In this subsection, we consider the vortices in the turbulent boundary layer. Since this flow is developing in the streamwise direction, it is more difficult to numerically simulate flow at sufficiently high Reynolds numbers than turbulent channel flow. Although we have employed numerical techniques (§ 2.4) such as a combination of two DNS [Fig. 2(c)] to overcome this difficulty, the achieved Taylor-length Reynolds number (7) of the simulated turbulence is $Re_\lambda \lesssim 75$ shown by squares in Fig. 3 even in the developed region where $Re_\theta = 3600$. Therefore, this is not fully developed turbulence (10) and the we cannot observe a power law of the energy spectrum shown by squares in Fig. 1.

We show the scale-decomposed vortices in Fig. 14(a), which was obtained by the method similar to those used for the turbulent wake (Figs. 10 and 11) and turbulent channel flow (Fig. 12). In Fig. 14(a), the red and yellow objects are vortices identified by isosurface of the second invariant (41) of velocity gradient tensor scale-decomposed at $\sigma^+ = 200$ and $\sigma^+ = 50$, respectively. Though we can observe coherent vortices at these two distinct scales, we cannot observe simple relationships, like in the turbulent channel flow [Fig. 12(b)], between vortices at these scales in the narrow logarithmic layer because of the smallness of the Reynolds number ($Re_\lambda \lesssim 75$ and $Re_\tau \lesssim 1380$).

Nevertheless, it is interesting to examine the quantity Γ defined by (53) in the previous subsection in this flow [Fig. 13(b)]. We can see the similar observations to the turbulent channel flow, though the logarithmic range is rather narrow (say, $100 \lesssim y^+ \lesssim 150$). More precisely, vortices smaller than the Corrsin length $L_c(y) \approx \kappa y$ (i.e. wall-detached eddies) are created by stretching by larger vortices, whereas vortices larger than L_c (i.e. wall-attached eddies) are directly created by mean flow. This implies that the hierarchy of vortices in turbulent channel flow and turbulent boundary layer may be sustained in a similar manner. Therefore, analyzing turbulence at higher Reynolds numbers (say, twice larger R_λ, which corresponds to about four times larger Re_θ), we may observe a hierarchical structure of coherent vortices even in the turbulent boundary layer.

It is further interesting to observe largest wall-attached eddies in the turbulent boundary layer. Red vortices shown in Fig. 14 are at the scale of $\sigma = 200\ell_\tau \approx 0.18\delta_{99} \approx 1.4\theta$. In other words, the vortices in Fig. 14 are the largest wall-attached eddies, which are obviously hairpin-shaped. Recall that, similarly to other turbulence, we cannot observe large-scale vortices by the visualization without scale decomposition [Fig. 5(e)]. Once we use the scale decomposition, it is easy to identify larger vortices. The difference is obvious by comparing the (red) large vortices shown in Fig. 14 and the fine vortices shown in Fig. 5(e); note that we visualize same flow at same location corresponding to $Re_\theta = 3200$–3800. Though there is no hairpin vortices at the smallest scale [Fig. 5(e)], there are many hairpins in largest scales (Fig. 14). Incidentally, the largest vortices in turbulent channel flow (i.e. red vortices shown in Fig. 12(a)) are not hairpin-like but many of them look like large streamwise longitudinal vortices. Although as examined in Fig. 13, these largest vortices are sustained by the direct action of the mean shear in both of these wall turbulence, their shape is different. This may be caused by the difference in the flow in the outer layer; namely, it is laminar in boundary layers and turbulent in channel flow.

5 Conclusions

From the beginning of this century, direct numerical simulations (DNS) of developed turbulence at high Reynolds numbers were extensively conducted by many authors. In this article, on the basis of our previous studies on the analysis of DNS data of turbulence in a periodic cube (Goto, 2008, 2012; Goto et al, 2017), turbulent wake behind a circular cylinder (Fujino et al, 2023), turbulent channel flow (Motoori and Goto, 2021), and turbulent boundary layer (Motoori and Goto, 2019, 2020), we have reviewed the knowledge about the hierarchy of coherent vortices in these turbulent flows.

In these DNS, a sufficiently large number of degrees of freedom are employed ($1024^3 \approx 10^9$ for the periodic turbulence, $8192 \times 2560 \times 1024 \approx 2 \times 10^{10}$ for the wake, $2048^2 \times 1081 \approx 4 \times 10^9$ for the channel flow, and $8064 \times 640 \times 768 \approx 4 \times 10^9$ for the boundary layer) so that we can numerically realize developed turbulence. More concretely, the Taylor-length Reynolds number (7), which is an indicator of the development of turbulence, is $Re_\lambda \approx 250$–320 (turbulence in a periodic cube), $Re_\lambda \lesssim 140$ (turbulent channel flow), $Re_\lambda \approx 100$ (turbulent wake behind a cylinder), $Re_\lambda \lesssim 75$ (turbulent boundary layer) see Fig. 3. According to the criterion (10), by Dimotakis (2000), examined flows are developed turbulence except for the boundary layer. In fact, we observe broad energy spectra (Fig. 1) for these flow, in which, therefore, there is a hierarchy of vortices with different sizes.

However, if we identify vortices in terms of the quantities related to the velocity gradient tensor, such as the enstrophy (40) or its second invariant (41), we always observe forests of fine-scale vortices (Fig. 5). This observation is explained by a simple argument given in § 3; since the energy spectrum obeys the $-5/3$ power law (2) of wavenumber in the inertial range (3), the velocity gradient is predominantly determined by the smallest scale eddies.

Therefore, as demonstrated in § 4, to capture the hierarchy of vortices with different sizes, we need scale decomposition of velocity fields. In the present study, we have shown that we use Fourier band-pass filter (46) for the periodic turbulence and the combination (51) of two Gaussian filters (50) in real space for the other cases to identify the hierarchy of coherent vortices shown in Figs. 6, 10, 11, 12, and 14. In other words, we only need a scale decomposition to observe the hierarchy of vortices.

In the periodic turbulence, the largest vortices are sustained by external force and their features depend on the force. Smaller vortices acquire their energy due to vortex stretching from larger vortices (Yoneda et al, 2022, Fig. 1). Created vortices are tubular and they tend to form counter-rotating pairs (Goto et al, 2017, Fig. 8). In fact, we can observe concrete examples that smaller vortices are created, by being stretched, in strain-rate field around a counter-rotating pair of larger vortex tubes (Figs. 7 and 8). Here, we reemphasize that since there coexist numerous vortices at different ages (Fig. 9) in statistically stationary turbulence, we observe clear events such as in these figures only when the moment of the birth of smaller vortices.

The sustaining mechanism of hierarchy of vortices in the turbulent wake behind a cylinder depends on the regions. In the recirculation region just behind the cylinder, turbulent twin vortices are stationary and they play a role similar to the turbulent Taylor–Green vortices in the flow examined in Fig. 7. This is the reason why we

observe similar hierarchy of coherent vortices in the recirculation region (Fig. 10). In the downstream region (Fig. 11), we observe clear successive creations of rib vortices around roller, i.e. shedding, vortices; and those of smaller vortices around rib vortices. We may also understand these events by the process of vortex stretching in strain-rate fields around larger counter-rotating vortex pairs. Since the moment of birth of smaller vortices is clear, these events are also clear in the downstream region of the wake.

For wall turbulence, we must consider the hierarchy of vortices depending on the distance y from the wall. We have demonstrated this by using the data (Fig. 13) of developed turbulent channel flow. The largest vortices (i.e. wall-attached eddies) at the distance y from the wall have a size comparable to y, and these vortices are directly created by being stretched by mean shear. On the other hand, smaller vortices (i.e. wall-detached eddies) are created by the similar process in turbulent in a periodic cube; namely, vortex stretching in strain-rate field around larger vortices. In fact we can find concrete events to support this picture (Fig. 12). We may also see that in the near-wall regions ($y^+ \lesssim 30$–100, the buffer layer), there exist only large vortices, which are sustained by interaction with mean flow fluctuation (i.e. streaks). Therefore, the energy cascade only takes place in logarithmic and outer layers, $y^+ \gtrsim 30$–100. This is consistent with the classical view that Kolmogorov (1941)'s similarity hypothesis holds for small vortices in regions away from solid walls.

We may explain the hierarchy of vortices and its sustaining mechanism in turbulent boundary layer in a similar manner to turbulent channel flow. More concretely, wall-attached eddies are directly created by mean shear flow, whereas smaller wall-detached eddies are created by the energy cascade process from larger eddies. Since the Reynolds number of examined turbulent boundary layer is low ($Re_\lambda \lesssim 75$), we cannot observe a self-similar hierarchical structure of vortices. Nevertheless, the Reynolds number is large enough to observe the scale separation between the smallest vortices [Fig. 5(e)] and the largest ones (Fig. 14). It is of importance to observe that the largest wall-attached eddies, which are captured by the scale-decomposition, are hairpin-shaped vortices (Fig. 14) even in the developed region. This obviation is consistent with previous experiments (Head and Bandyopadhyay, 1981; Adrian et al, 2000).

As demonstrated above, for many kinds of canonical flows, DNS of fully developed turbulence, which satisfy the criterion (10), are feasible. Thanks to this situation, we may develop detailed analysis which may reveal the origin of small-scale universality (Kolmogorov, 1941). Recall that we can also confirm this small-scale similarity in the energy spectrum shown in Fig. 1. In next a few decades, DNS of turbulence at further higher Reynolds numbers will be conducted to show these similarity more clearly. In other words, such DNS may not change the demonstrated picture in a qualitative manner. Therefore, the next targets of turbulence research are shifting to turbulence of more complex fluids such as magneto-hydrodynamic, non-Newtonian, or multiphase fluids.

Acknowledgments

We thank Dr Lozano-Durán and Prof Jiménez for providing us with their turbulent channel data. The DNS were conducted under the supports of the NIFS Collaboration Research Programs (08KTBL006, 11KNSS023, 13KNSS043, 15KNSS066,

17KNSS101, 18KNSS108, 20KNSS145, 22KISS010) and the HPCI System Research projects (hp210207, hp210075, hp220232). Our studies were partly supported by JSPS Grants-in-Aids for Scientific Research (16H04268, 20H02068, 20H01819, 20J10399, 21K20403, 23K13253).

Declarations

On behalf of all authors, the corresponding author states that there is no conflict of interest.

References

Abe H, Kawamura H, Matsuo Y (2001) Direct numerical simulation of a fully developed turbulent channel flow with respect to the reynolds number dependence. J Fluids Eng 123:382–393

Adrian RJ, Meinhart CD, Tomkins CD (2000) Vortex organization in the outer region of the turbulent boundary layer. J Fluid Mech 422:1–54

Batchelor GK (1953) The theory of homogeneous turbulence. Cambridge Univ. Press.

Biferale L (2003) Shell models of energy cascade in turbulence. Ann Rev Fluid Mech 35:441–468

Borue V, Orszag SA (1998) Local energy flux and subgrid-scale statistics in three-dimensional turbulence. J Fluid Mech 366:1–31

Brenner MP, Hormoz S, Pumir A (2016) Potential singularity mechanism for the euler equations. Phys Rev Fluids 1:084503

Canuto C, Hussaini MY, Quarteroni A, et al (2006) Spectral Methods. Springer

Carbone M, Bragg AD (2020) Is vortex stretching the main cause of the turbulent energy cascade? J Fluid Mech 883:R2

Cardesa JI, Alberto VM, Jiménez J (2017) The turbulent cascade in five dimensions. Science 357:782

Davidson PA (2004) Turbulence—An introduction for scientists and engineers. Oxford Univ. Press.

Davidson PA, Morishita K, Kaneda Y (2008) On the generation and flux of enstrophy in isotropic turbulence. J Turb p N42

del Álamo JC, Jiménez J (2003) Spectra of the very large anisotropic scales in turbulent channels. Phys Fluids 15:L41–L44

del Álamo JC, Jiménez J, Zandonade P, et al (2004) Scaling of the energy spectra of turbulent channels. J Fluid Mech 500:135–144

Dimotakis PE (2000) The mixing transition in turbulent flows. J Fluid Mech 409:69–98

Doan NA, Swaminathan N, Davidson PA, et al (2018) Scale locality of the energy cascade using real space quantities. Phys Rev Fluids 3:084601.

Domaradzki JA, Rogallo RS (1990) Local energy transfer and nonlocal interactions in homogeneous, isotropic turbulence. Phys Fluids A 2:413–426

Eitel-Amor G, Örlü R, Schlatter P (2014) Simulation and validation of a spatially evolving turbulent boundary layer up to Re_θ=8300. Int J Heat Fluid Flow 47:57–69

Eitel-Amor G, Örlü R, Schlatter P, et al (2015) Hairpin vortices in turbulent boundary layers. Phys Fluids 27:025108

Frisch U (1995) Turbulence, The Legacy of A. N. Kolmogorov. Cambridge Univ. Press

Fujino J, Motoori Y, Goto S (2023) Hierarchy of coherent vortices in turbulence behind a cylinder. J Fluid Mech 975

Goto S (2008) A physical mechanism of the energy cascade in homogeneous isotropic turbulence. J Fluid Mech 605:355–366

Goto S (2012) Coherent structures and energy cascade in homogeneous turbulence. Prog Theo Phys Suppl 195:139–156

Goto S, Saito Y, Kawahara G (2017) Hierarchy of antiparallel vortex tubes in spatially periodic turbulence at high reynolds numbers. Phys Rev Fluids 2:064603

Hamilton JM, Kim J, Waleffe F (1995) Regeneration mechanisms of near-wall turbulence structures. J Fluid Mech 287:317–348

Head M, Bandyopadhyay P (1981) New aspects of turbulent boundary-layer structure. J Fluid Mech 107:297–338

Hoyas S, Jiménez J (2006) Scaling of the velocity fluctuations in turbulent channels up to $Re_\tau = 2003$. Phys Fluids 18:011702

Hoyas S, Oberlack M, Alcántara-Ávila F, et al (2022) Wall turbulence at high friction Reynolds numbers. Phys Rev Fluids 7:014602

Hussain F (1986) Coherent structures and turbulence. J Fluid Mech 173:303–356

Hussain F, Duraisamy K (2011) Mechanics of viscous vortex reconnection. Phys Fluids 23:021701

Hwang J, Lee J, Sung HJ, et al (2016) Inner-outer interactions of large-scale structures in turbulent channel. J Fluid Mech 790:128–157

Hwang Y, Bengana Y (2016) Self-sustaining process of minimal attached eddies in turbulent channel flow. J Fluid Mech 795:708–738

Ishihara T, Kaneda Y, Morishita K, et al (2020) Second-order velocity structure functions in direct numerical simulations of turbulence with R_λ up to 2250. Phys Rev Fluids 5:104608

Johnson PL (2020) Energy transfer from large to small scales in turbulence by multiscale nonlinear strain and vorticity interactions. Phys Rev Lett 124:104501

Johnson PL (2021) On the role of vorticity stretching and strain self-amplification in the turbulence energy cascade. J Fluid Mech 922:A3

Kajishima T, Taira K (2017) Computational Fluid Dynamics: Incompressible Turbulent flows. Springer

Kaneda Y, Ishihara T, Yokokawa M, et al (2003) Energy dissipation rate and energy spectrum in high resolution direct numerical simulations of turbulence in a peridic box. Phys Fluids 15:L21–L24

Kempe T, Fröhlich J (2012) An improved immersed boundary method with direct forcing for the simulation of particle laden flows. J Comput Phys 231:3663

Kerr RM (2013) Swirling, turbulent vortex rings formed from a chain reaction of reconnection events. Phys Fluids 25:065101

Khujadze G, Oberlack M (2004) DNS and scaling laws from new symmetry groups of ZPG turbulent boundary layer flow. Theo Comput Fluid Dyn 18:391–411

Kida S, Miura H (1998) Swirl condition in low-pressure vortex. J Phys Soc Japan 67:2166–2169

Kim J, Moin P, Moser R (1987) Turbulence statistics in fully developed channel flow at low reynolds number. J Fluid Mech 177:133–166

Kim KC, Adrian RJ (1999) Very large-scale motion in the outer layer. Phys Fluids 11:417–422

Kline SJ, Reynolds WC, Schraub F, et al (1967) The structure of turbulent boundary layers. J Fluid Mech 30:741–773

Kolmogorov AN (1941) The local structure of turbulence in incompressible viscous fluid for very large reynolds numbers. Dokl Akad Nauk SSSR 30:301–305. English translation in Proc. Roy. Soc. London, Ser. A **434**, 9–13 (1991)

Komminaho J, Skote M (2002) Reynolds stress budgets in Couette and boundary layer flows. Flow, Turbulence and Combustion 68:167–192

Lamorgese AG, Caughey DA, Pope SB (2005) Direct numerical simulation of homogeneous turbulence with hyperviscosity. Phys Fluids A 17:015106

Lee J, Lee JH, Choi JI, et al (2014) Spatial organization of large- and very-large-scale motions in a turbulent channel flow. J Fluid Mech 749:818–840

Lee J, Sung HJ, Zaki TA (2017) Signature of large-scale motions on turbulent/non-turbulent interface in boundary layers. J Fliud Mech 819:165–187

Lele SK (1992) Compact finite difference schemes with spectral-like resolution. J Comput Phys 103:16–42

Leung T, Swaminathan N, Davidson PA (2012) Geometry and interaction of structures in homogeneous isotropic turbulence. J Fluid Mech 710:453–481

Lozano-Durán A, Jiménez J (2014) Effect of the computational domain on direct simulations of turbulent channels up to $Re_\tau = 4200$. Phys Fluids 26:011702

Lozano-Durán A, Holzner M, Jiménez J (2016) Multiscale analysis of the topological invariants in the logarithmic region of turbulent channels at a friction Reynolds number of 932. J Fluid Mech 803:356–394

Ma X, Karamanos GS, Karniadakis G (2000) Dynamics and low-dimensionality of a turbulent near wake. J Fluid Mech 410:29–65

Marusic I, Monty JP (2019) Attached eddy model of wall turbulence. Ann Rev Fluid Mech 51:49–74

McKeown R, Ostilla-Mónico R, Pumir A, et al (2018) Cascade leading to the emergence of small structures in vortex ring collisions. Phys Rev Fluids 3:124702

McKeown R, Ostilla-Mónico R, Pumir A, et al (2020) Turbulence generation through an iterative cascade of the elliptical instability. Science Advances 6:eaaz2717

McKeown R, Pumir A, Rubinstein SM, et al (2023) Energy transfer and vortex structures: visualizing the incompressible turbulent energy cascade. New J Phys 25:103029

Melander MV, Hussain F (1988) Cut-and-connect of two antiparallel vortex tubes. Stanford Univ, Proceedings of the 1988 Summer Program pp 257–286

Melander MV, Hussain F (1993) Coupling between a coherent structure and fine-scale turbulence. Phys Rev E 48:2669–2689

Miura H, Kida S (1997) Identification of tubular vortices in turbulence. J Phys Soc Japan 66:1331–1334

Motoori Y, Goto S (2019) Generation mechanism of a hierarchy of vortices in a turbulent boundary layer. J Fluid Mech 865:1085–1109

Motoori Y, Goto S (2020) Hairpin vortices in the largest scale of turbulent boundary layers. Int J Heat Fluid Flow 86:108658

Motoori Y, Goto S (2021) Hierarchy of coherent structures and real-space energy transfer in turbulent channel flow. J Fluid Mech 911:A27

Ohkitani K, Kida S (1992) Triad interactions in a forced turbulence. Phys Fluids A 4:794–802

Orszag SA (1971) Accurate solution of the orr–sommerfeld stability equation. J Fluid Mech 50:689–703

Orszag SA, Patterson GS (1972) Numerical simulation of three-dimensional homogeneous isotropic turbulence. Phys Rev Lett 28:76–79

Paul I, Papadakis G, Vassilicos J (2017) Genesis and evolution of velocity gradients in near-field spatially developing turbulence. J Fluid Mech 815:295–332

Richardson LF (1922) Weather Prediction by Numerical Process. Cambridge Univ. Press.

Sagaut P, Cambon C (2018) Homogeneous turbulence dynamics, 2nd Edition. Springer

Schlatter P, Örlü R (2010) Assessment of direct numerical simulation data of turbulent boundary layers. J Fluid Mech 659:116–126

Schlatter P, Li Q, Örlü R, et al (2014) On the near-wall vortical structures at moderate Reynolds numbers. European J Mech B/Fluids 48:75–93

Sillero JA, Jiménez J, Moser RD (2013) One-point statistics for turbulent wall-bounded flows at Reynolds numbers up to $\delta^+ \approx 2000$. Phys Fluids 25:105102

Simens MP, J. J, S. H, et al (2009) A high-resolution code for turbulent boundary layers. J Comput Phys 228:4218–4231

Spalart PR (1988) Direct simulation of a turbulent boundary layer up to $R_\theta = 1410$. J Fluid Mech 187:61–98

Sreenivasan KR (1995) On the universality of the kolmogorov constant. Phys Fluids 7:2778–2784

Tanahashi M, Kang SJ, Miyamoto T, et al (2004) Scaling law of fine scale eddies in turbulent channel flows up to Re_τ= 800. International journal of heat and fluid flow 25:331–340

Taylor GI (1935) Statistical theory of turbulence. Proc Roy Soc A 151:421–444

Taylor GI (1938) Production and dissipation of vorticity in a turbulent fluid. Proc Roy Soc London A 164:15–23

Tennekes H, Lumley JL (1972) A First Course in Turbulence. M.I.T. Press, Cambridge, Mass.

Tomboulides A, Orszag S, Karniadakis G (1993) Direct and large-eddy simulations of axisymmetric wakes. In: 31st Aerospace Sciences Meeting, p 546

Tsinober A (2001) An informal introduction to turbulence. Kluwer Academic Publishers

Tsuruhashi T, Goto S, Oka S, et al (2022) Self-similar hierarchy of coherent tubular vortices in turbulence. Phil Tran Roy Soc A 380:20210053

Uhlmann M (2005) An immersed boundary method with direct forcing for the simulation of particulate flows. J Comput Phys 209:448

Vela-Martín A, Jiménez J (2021) Entropy, irreversibility and cascades in the inertial range of isotropic turbulence. J Fluid Mech 915:A36

Yamada M, Ohkitani K (1987) Lyapunov spectrum of a chaotic model of three-dimensional turbulence. J Phys Soc Japan 56:4210–4213

Yamamoto Y, Tsuji Y (2018) Numerical evidence of logarithmic regions in channel flow at Re_τ= 8000. Phys Rev Fluids 3:012602

Yao H, Schnaubelt M, Szalay AS, et al (2024) Comparing local energy cascade rates in isotropic turbulence using structure-function and filtering formulations. J Fluid Mech 980:A42

Yao J, Hussain F (2020) A physical model of turbulence cascade via vortex reconnection sequence and avalanche. J Fluid Mech 883:A51

Yasuda T, Goto S, Vassilicos JC (2020) Formation of power-law scalings of spectra and multiscale coherent structures in near-field of grid-generated turbulence. Phys Rev Fluids 5:014601

Yoneda T, Goto S, Tsuruhashi T (2022) Mathematical reformulation of the Kolmogorov-Richardson energy cascade in terms of vortex stretching. Nonlinearity 35:1380–1401